Cell Reports
Medicine

Article

TNF-α-mediated myeloid-instructed CD14⁺CD4⁺ T cells are associated with poor survival in lung adenocarcinoma

Graphical abstract

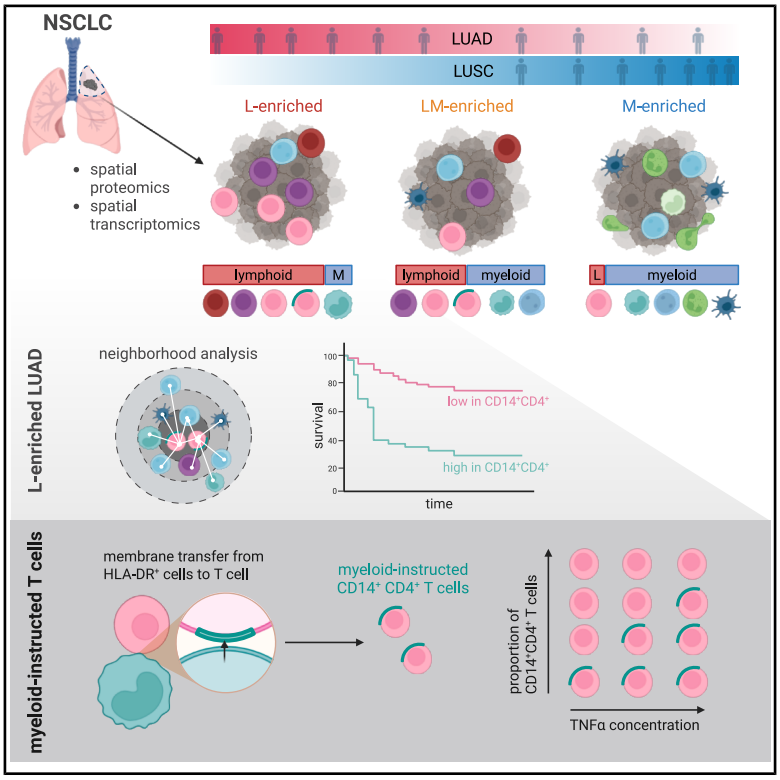

Authors

Claire Marceaux, Ilariya Tarasova, Daniel Batey, ..., Kelly L. Rogers, Belinda Phipson, Marie-Liesse Asselin-Labat

Correspondence

labat@wehi.edu.au

In brief

Marceaux et al. uncover a TNF-α-driven mechanism of immune suppression in lung cancer. Their spatial multi-omics analysis shows that myeloid-T cell interactions generate hybrid immune cells that weaken anti-tumor responses, revealing how inflammatory signaling rewires the tumor microenvironment to promote disease progression.

Highlights

- Immune cell infiltration subtypes are independent of oncogenic driver status
- Myeloid-instructed CD14⁺CD4⁺ T cells arise through trogocytosis
- T cell trogocytosis is augmented by TNF-α
- High infiltration of CD14⁺CD4⁺ T cells correlates with poor survival

Marceaux et al., 2026, Cell Reports Medicine 7, 102593
February 17, 2026
https://doi.org/10.1016/j.xcrm.2026.102593

CellPress

Cell Reports Medicine

CellPress
OPEN ACCESS

Article

TNF-α-mediated myeloid-instructed CD14+CD4+ T cells are associated with poor survival in lung adenocarcinoma

Claire Marceaux,[1,4] Ilariya Tarasova,[3] Daniel Batey,[1] Kenta Yokote,[1] Velimir Gayevskiy,[1] Reema Jain,[1,4] Marina Leiwe,[1,4] Laurie Choux,[1] Lucy Riley,[1] Nina Tubau Ribera,[2] Edward Yang,[3] Jack Hywood,[7] Michael Christie,[7] Phillip Antippa,[6,7] Terence P. Speed,[3,5] Kelly L. Rogers,[2,4] Belinda Phipson,[3,4] and Marie-Liesse Asselin-Labat[1,4,8,*]

[1]Personalised Oncology Division, The Walter and Eliza Hall Institute of Medical Research, Parkville, VIC, Australia
[2]Advanced Technology and Biology Division, The Walter and Eliza Hall Institute of Medical Research, Parkville, VIC, Australia
[3]Bioinformatics Division, The Walter and Eliza Hall Institute of Medical Research, Parkville, VIC, Australia
[4]Department of Medical Biology, The University of Mebourne, Parkville, VIC, Australia
[5]School of Mathematics and Statistics, The University of Melbourne, Parkville, VIC, Australia
[6]Department of Surgery, The University of Melbourne, Parkville, VIC, Australia
[7]The Royal Melbourne Hospital, Parkville, VIC, Australia
[8]Lead contact
*Correspondence: labat@wehi.edu.au
https://doi.org/10.1016/j.xcrm.2026.102593

SUMMARY

The tumor microenvironment is composed of diverse immune populations that can either support anti-tumor immunity or promote tumor progression. Myeloid cells are major drivers of immunosuppression, yet therapies targeting them have shown limited success. To uncover mechanisms underlying myeloid-driven immune suppression, we performed spatial multi-omics analyses of non-small cell lung cancer (NSCLC). Independent of oncogenic driver status, tumors stratify into lymphoid-enriched, myeloid-enriched, and mixed immune-infiltrated subtypes. In tumor and adjacent non-malignant lungs, we identify myeloid-instructed CD14+CD4+ T cells. These cells arise through trogocytosis adopting an atypical phenotype. In lymphoid-enriched tumors, high infiltration of CD14+CD4+ T cells correlates with poor patient survival. Spatial transcriptomics reveal enrichment of tumor necrosis factor alpha (TNF-α) signaling in CD14+CD4+-T-cell-rich tumors. Functional assays demonstrate that TNF-α enhanced trogocytosis, promoting the formation of CD14+CD4+ T cells. These findings uncover a TNF-α-mediated mechanism of immunosuppression in the TME and highlight aberrant myeloid-T cell interactions as contributors to NSCLC progression.

INTRODUCTION

Histopathological analysis of cancer specimens is an essential part of clinical diagnosis to inform therapeutic decisions. Tissue architecture and cellular organization provide a layer of information critical for pathologists to make informed diagnoses. Similarly, the characterization of immune cell phenotypes and functional states in the physical context of a tumor is necessary to gain a broad understanding of cancer immunology. This knowledge is essential in non-small cell lung cancer (NSCLC) where immunotherapy has improved patient outcomes as single agent or in combination with chemotherapy. Yet, a number of patients do not respond to these treatments.[1,2] A comprehensive mapping of the complexity and heterogeneity of the cellular interactions in the tumor microenvironment (TME) driving tumor progression and relapse is still lacking, hindering the development of therapies tailored to the specific characteristics of individual tumor ecosystems.

Tumor cell molecular characteristics such as tumor mutational burden (TMB) and programmed death ligand 1 (PDL1) expression are still heavily relied upon to determine patient prognostic and therapeutic approaches.[3,4] However, recent studies demonstrate the importance of assessing the immune contexture to understand tumor evolution[5,6] and for prognostic and therapeutic purposes.[7,8] Evaluation of immune cell composition and activity in NSCLC have been performed in small patient cohorts using single-cell transcriptomics combined with cell surface protein analyses.[9–12] Detailed evaluation of individual tumor cells and immune cells determined that the intersection between tumor cell-intrinsic factors, such as *TP53* mutation and TMB, combined with immune cell characteristics may be used to better predict response to immunotherapeutics.[12] However, these studies lack spatial resolution and information on how immune cell communities may influence immune and tumor cell behaviors. Recent work by Sorin et al. utilized imaging mass cytometry to profile the TME in LUAD and revealed that specific immune cell neighborhoods composed of B cells and T helper cells were associated with better patient outcomes.[13] Further analyses by this group to compare LUAD and LUSC spatial architecture demonstrated the interactions between myeloid and lymphoid cells as a prominent feature of LUAD.[14] These studies

highlight how cellular communities and their specific location, identified through spatial analysis, have a stronger biological impact than individual cells. Evaluating this spatial organization provides a new layer of information, akin to that utilized in anatomical pathology for diagnosis, to decipher tumor biology.

Tumor-infiltrating myeloid-derived monocytes or neutrophils, called myeloid-derived suppressor cells, and tumor-associated macrophages are key drivers of immunosuppression in cancer.[15,16] While the role of myeloid cells in blocking anti-tumor immunity has been recognized for a long time, there has been limited success in large-scale clinical trials of therapies that modulate myeloid cell function.[17] Preclinical and translational studies in organ-specific tumor contexts are essential in understanding the many mechanisms by which myeloid cells drive immunosuppression in the TME and exploiting myeloid cell vulnerabilities to increase the success of myeloid-targeted therapies. Recent studies have highlighted that myeloid-cell-mediated immunosuppression can be initiated in early myeloid cell progenitor cells in the bone marrow,[18] as well as locally, within the TME, through the instruction of lymphoid cells.[19] LaMarche et al.[18] showed that basophil-derived interleukin (IL)-4 reprogrammed myeloid progenitor cells in the bone marrow of NSCLC tumor-bearing mice, supporting the differentiation of tumor-promoting myeloid cells. Depleting IL-4 signaling in myeloid progenitor cells in the bone marrow using conditional knockout mice reduced tumor burden.[18] Systemic inhibition of IL-4 with Dupilumab in combination with immune checkpoint inhibitors reduced circulating monocytes and increased $CD8^+$ T cell infiltration in a small clinical trial,[18] demonstrating the effect of tumor cells beyond the local TME.

The impact of myeloid cells in modulating local adaptive immunity was evaluated by Pallett et al.[19] where they described a subset of myeloid-instructed tissue-resident T cells present in the skin, lymph nodes, and liver. They showed that a subset of $CD8^+$, and in lower abundance $CD4^+$ T cells, expressed the Toll-like receptor 4 (TLR4) coreceptor CD14, a canonical marker of myeloid cells and innate immunity.[19] These myeloid-instructed T cells were reprogrammed by the transfer of myeloid material to T cells upon direct contact between T cells and mononuclear phagocytes and were found to accumulate in hepatitis-B-virus-infected livers and in hepatocarcinomas. The existence and contribution of these myeloid-instructed T cells to anti-tumor immunity in solid tumors is still unknown.

Here, we applied multiplex ion beam imaging (MIBIscope) and spatial transcriptomic (GeoMx) to a clinically annotated cohort of NSCLC patient samples to identify cellular and molecular events controlling anti-tumor immunity. We demonstrated the existence of a subset of clonally expanded T cells expressing the myeloid marker CD14. Analysis of three distinct cohorts of NSCLC confirmed the existence of this discrete T cell subset in tumors and showed that high infiltration of $CD14^+CD4^+$ T cells in the tumor core in lymphoid-enriched cancers correlated with short-term patient survival. $CD4^+$ T cells acquired CD14 from myeloid cells by trogocytosis, resulting in an atypical T cell phenotype. Tumors enriched in myeloid-instructed $CD14^+CD4^+$ T cells exhibited an upregulation of genes in the tumor necrosis factor alpha (TNF-α) signaling pathway. We showed that TNF-α increased $CD4^+$ T cell trogocytosis, augmenting the proportions of myeloid-instructed T cells. TNF-α is known to exert a number of pro-tumorigenic activities.[20,21] Here, we show that TNF-α-induced trogocytosis and myeloid instruction of T cells may be an additional mechanism by which TNF-α reduces anti-tumor immunity.

RESULTS

A longitudinal cohort of resected NSCLC with survival outcome

To study the features of anti-tumor immunity associated with patient outcome in resectable NSCLC, we utilized a bank of 136 treatment-naïve NSCLC samples (stage I–IIIa) for which we had up to 10 years of longitudinal clinical follow-up (Figure 1A). To characterize the cellular traits of the TME that may be associated with short or prolonged survival, we selected tissue samples from patients with an overall survival of less than 3 years or more than 6 years post-surgery to perform spatial proteomics and spatial transcriptomics analyses. A total of 68 patients were analyzed, comprising 28 samples with less than 3 years survival (21 LUAD and 7 LUSC) and 40 samples (26 LUAD and 14 LUSC) with more than 6 years survival (Figure 1A). H&E images were annotated by a pathologist to select regions of interest (ROIs) for spatial single-cell proteomics using the MIBIscope and spatial transcriptomics using whole transcriptome profiling on the GeoMx. On each ROI, GeoMx enabled the analysis of the gene expression profile of tumor cells exclusively (area of illumination [AOI] $panCK^+$ cells) and the immune compartment (AOI $CD45^+$ cells) (Figure 1B). After quality control checks, a total of 920 field of views for MIBI (FOVs: 400 × 400 μm, average of five per patient) and 234 matched AOIs (average of four per patient) on GeoMx were selected for further analysis corresponding to 64 patients (44 LUAD and 20 LUSC; Figure 1A; Tables S1 and S2).

For spatial proteomic analysis with MIBI, a bespoke panel of 38 conjugated antibodies was developed to identify tumor cells, immune cells, and fibroblasts and detail their functional state (Figure S1). Spatial analysis of cell communities in different tumor compartments (core, border, and stroma) were classified based on a pixel classifier trained in QuPath[22] (Figure 1B). Using a XGboost machine learning method to classify cells, a total of 384,808 cells were classified into epithelial cells, fibroblasts, and 10 major immune cell subpopulations: B cells, $CD4^+$ conventional T cells, $CD8^+$ T cells, $CD4^+$ regulatory T cells (Tregs), natural killer cells, gamma-delta T cells, macrophages, neutrophils, mast cells, and dendritic cells. A strong correlation between cell classification and the expression of expected markers was observed (Figure 1C). Classified cells corresponded to 73% tumor cells, 21% immune cells, and 6% stromal cells. Unsupervised clustering of immune cells demonstrated the performance of our classification model, with all lymphoid cells clustering away from myeloid cell subsets (Figure 1D). Consistent with previous publications utilizing *in situ* methods or tissue dissociation approaches,[5,11,13,23] the five most abundant immune cell types infiltrating NSCLC samples were B cells, $CD4^+$ conventional T cells, $CD8^+$ T cells, macrophages, and neutrophils (Figure 1C).

Overall, we exploited a cohort of clinically annotated NSCLC samples to develop methods for tissue and cell-type

CellPress
OPEN ACCESS

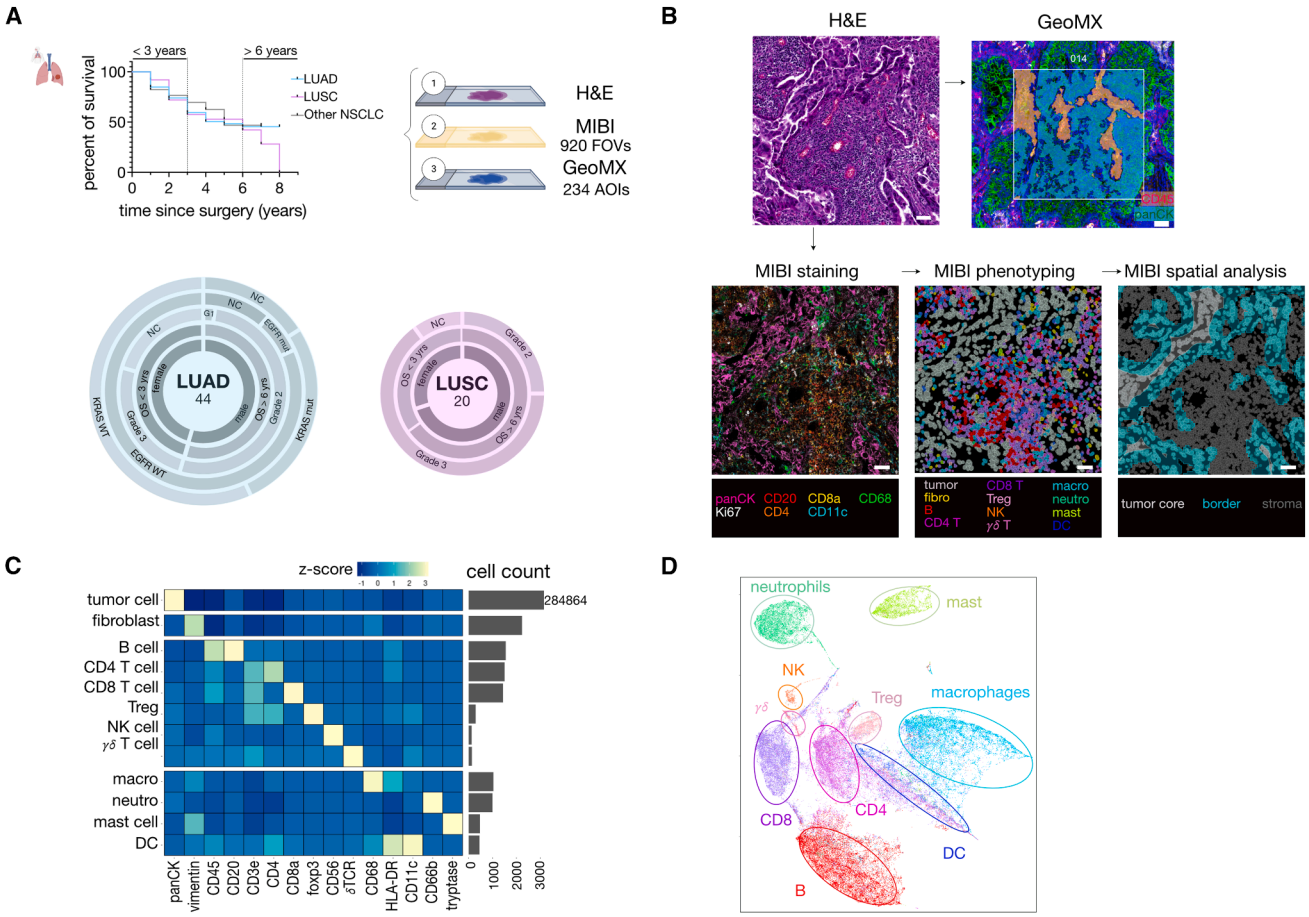

Figure 1. Spatial analysis of the tumor microenvironment and tumor cells in human non-small cell lung cancer samples

(A) Top: Kaplan-Meier survival curve showing overall survival of resected non-small cell lung cancer (NSCLC) sample cohort. MIBI, multiplex ion beam imaging spatial proteomics; GeoMX, spatial transcriptomics. Bottom: donuts graph representing the characteristics of the lung adenocarcinoma (LUAD) and squamous cell carcinoma (LUSC) patients analyzed. G: grade; NC: not cited.

(B) Spatial analysis workflow. Scale bars: 50 μm.

(C) Heatmap depicting the mean expression of each marker *Z* score normalized across all cell types.

(D) UMAP of immune cell types generated in all samples using the mean intensity measurement of each classification marker in all immune cells. See also Figure S1 and Tables S1 and S2.

classification from single-cell multiplex protein imaging and to interrogate the association between spatial proteomics and transcriptomics data with clinical outcomes.

DISTINCT SPATIAL CLUSTERS OF IMMUNE CELLS IN THE TME OF LUAD AND LUSC

We first investigated the characteristics of the tumor cells in LUAD and LUSC tissues. Consistent with previous studies,[24,25] GeoMX analysis of panCK$^+$ tumor cell regions showed clear transcriptomic differences between LUAD and LUSC tumor cells as well as heterogeneity in the gene expression profile of tumor cells between patients of the same histological subtypes (Figure 2A). LUAD and LUSC expressed typical phenotypic markers of each histological subtypes (e.g., *NKX2.1*, *KRT7*, *MUC1*, and *SFTPB* in LUAD and *KRT5*, *KRT6*, and *TP63* in LUSC; Figure S2A). With the proteomics analysis, we refined the co-expression of distinct functional markers in individual tumor cells. We observed a heterogeneous pattern of expression of major histocompatibility complex (MHC) class I and MHC class II in the two cancer subtypes (Figure 2B), consistent with previous studies where ~50% of tumors were found to have lost or had low levels of MHC class I and MHC class II.[26,27] MHC class I and MHC class II expressions were positively correlated in LUAD (Spearman correlation score: 0.7). Interestingly, loss of MHC class I was often associated with reduced expression of interferon gamma (IFN-γ) (Spearman correlation score: 0.49) in LUAD tumor cells but not in LUSC (Figure 2B). In LUSC, MHC class II expression was negatively associated with Ki67 expression (Spearman correlation score: −0.49). Expression of PDL1 in tumor cells varied across patients but was consistently lost in MHC class I negative tumors (Spearman correlation score: 0.32 in LUAD). IFN-γ expression was low in all LUSC samples, except for one patient, whereas ~50% of LUAD tumors expressed IFN-γ (Figure 2B). In

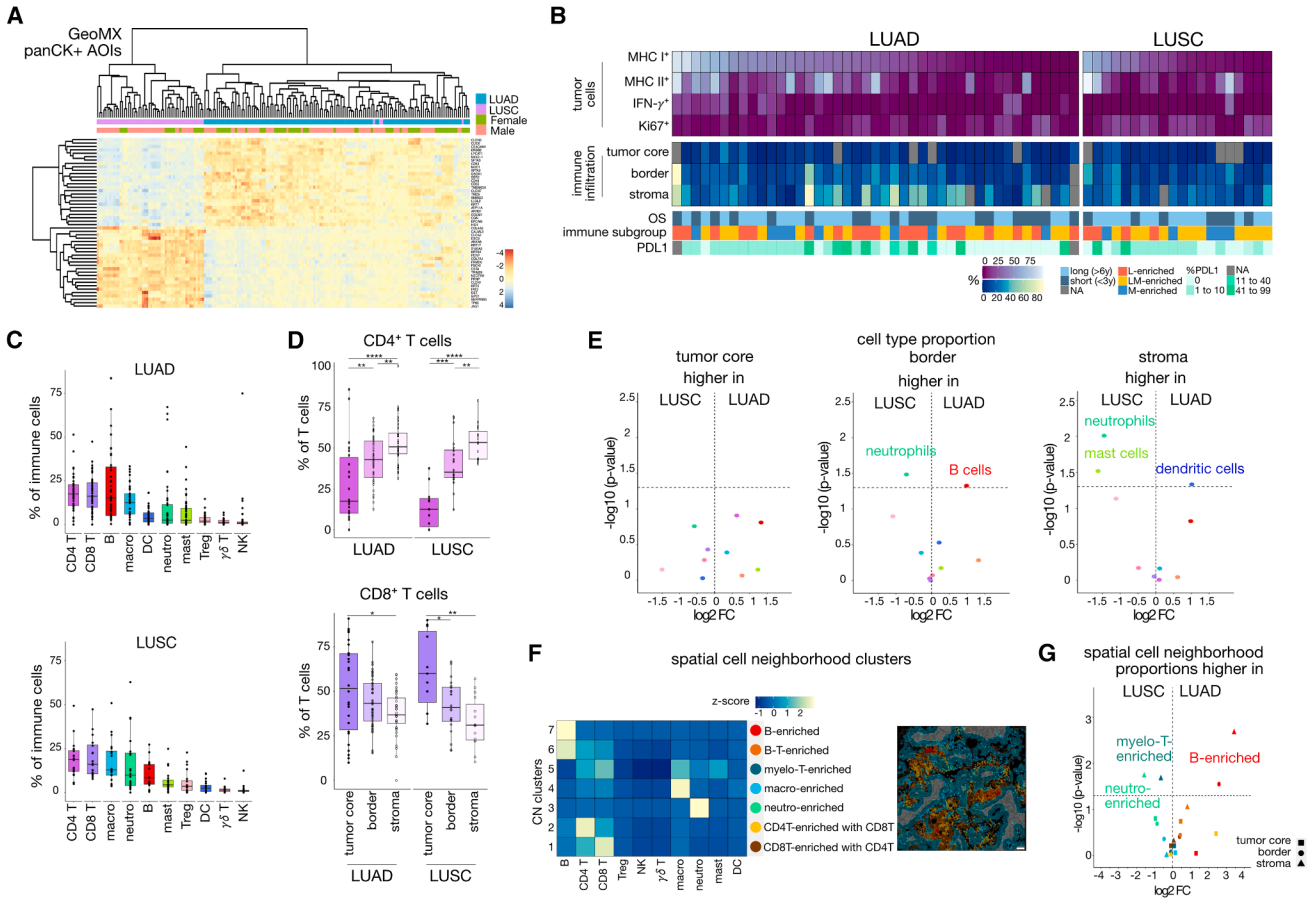

Figure 2. Cell communities containing myeloid cells are a feature of the LUSC TME

(A) Heatmap showing the expression of the top 50 differentially expressed genes in cytokeratin-positive tumor cells (panCK$^+$ AOI as measured with GeoMx) between LUAD and LUSC. Data show *Z* scores. *n* = 44 LUAD; *n* = 20 LUSC.

(B) Top: heatmap depicting the proportion of MHC I$^+$, MHC II$^+$, IFNγ$^+$, and Ki67$^+$ in tumor cells (PanCK$^+$) in individual patient samples from MIBI analysis. Middle: heatmap representing the proportion of immune cell infiltration in the three tissue compartments. OS: overall survival. *n* = 44 LUAD; *n* = 20 LUSC.

(C) Proportion of the different immune cell types in LUAD and LUSC, as determined by MIBI. Data show median ± SD. *n* = 44 LUAD; *n* = 20 LUSC.

(D) Boxplots showing the localization of CD4$^+$ T cells and CD8$^+$ T cells in the different spatial tissue compartments in LUAD and LUSC patients. Data show median ± SD. ****$p < 0.0001$; ***$p < 0.001$; **$p < 0.01$; *$p < 0.05$ comparing the different compartments, Wilcoxon test. *n* = 44 LUAD; *n* = 20 LUSC.

(E) Volcano plots comparing the proportion of each immune cell subtype in LUAD and LUSC samples. A horizontal dashed line indicates −log10(0.05), Wilcoxon test. *n* = 44 LUAD; *n* = 20 LUSC.

(F) Heatmap showing seven cell neighborhoods (CN) detected in NSCLC samples. Right panel: representative images showing rendering of different CN in tumor core (gray), border (blue), and stroma (dark gray). Scale bars: 50 μm.

(G) Volcano plots comparing the proportion of each CN cluster between LUAD and LUSC samples. Wilcoxon test. *n* = 44 LUAD; *n* = 20 LUSC. See also Figure S2.

LUAD, MHC-I/II^{low} tumors had less immune cell infiltration in the tumor core or border than MHC class I/class II^{high} tumors. The tumor-cell-specific expression of each of these markers, including PDL-1, was not associated with relapse-free survival or overall survival (Figures 2B and S2B).

We then compared the immune microenvironment of LUAD and LUSC samples. In both tumor subtypes, the predominant immune subsets in the whole tissue were CD4$^+$ and CD8$^+$ T cells, followed by B cells in LUAD and macrophages in LUSC (Figure 2C). Analysis of the specific location of the cells in different tumor compartments (core, border, or stroma) showed that immune cells were more frequent in the stroma (Figure S2C). Within the immune cells, the proportions of distinct immune subsets were evenly distributed between the compartments or enriched in the stroma, except for macrophages and CD8$^+$ T cells that were more frequently detected in the tumor core and at the tumor border, in both LUAD and LUSC (Figures 2D and S2D). Whole tissue analysis of immune cell infiltration revealed significantly higher B cell infiltration in the LUAD TME compared with LUSC, whereas neutrophils were more often present in LUSC (Figure S2E). Detailed analysis of the TME in different compartments of the tumors highlighted that the enrichment for B cells in LUAD occurred at the border of the tumor front, while neutrophils were located at the border and in the stroma of LUSC (Figure 2E). In addition, this analysis of the different tumor compartments highlighted further differences

CellPress
OPEN ACCESS

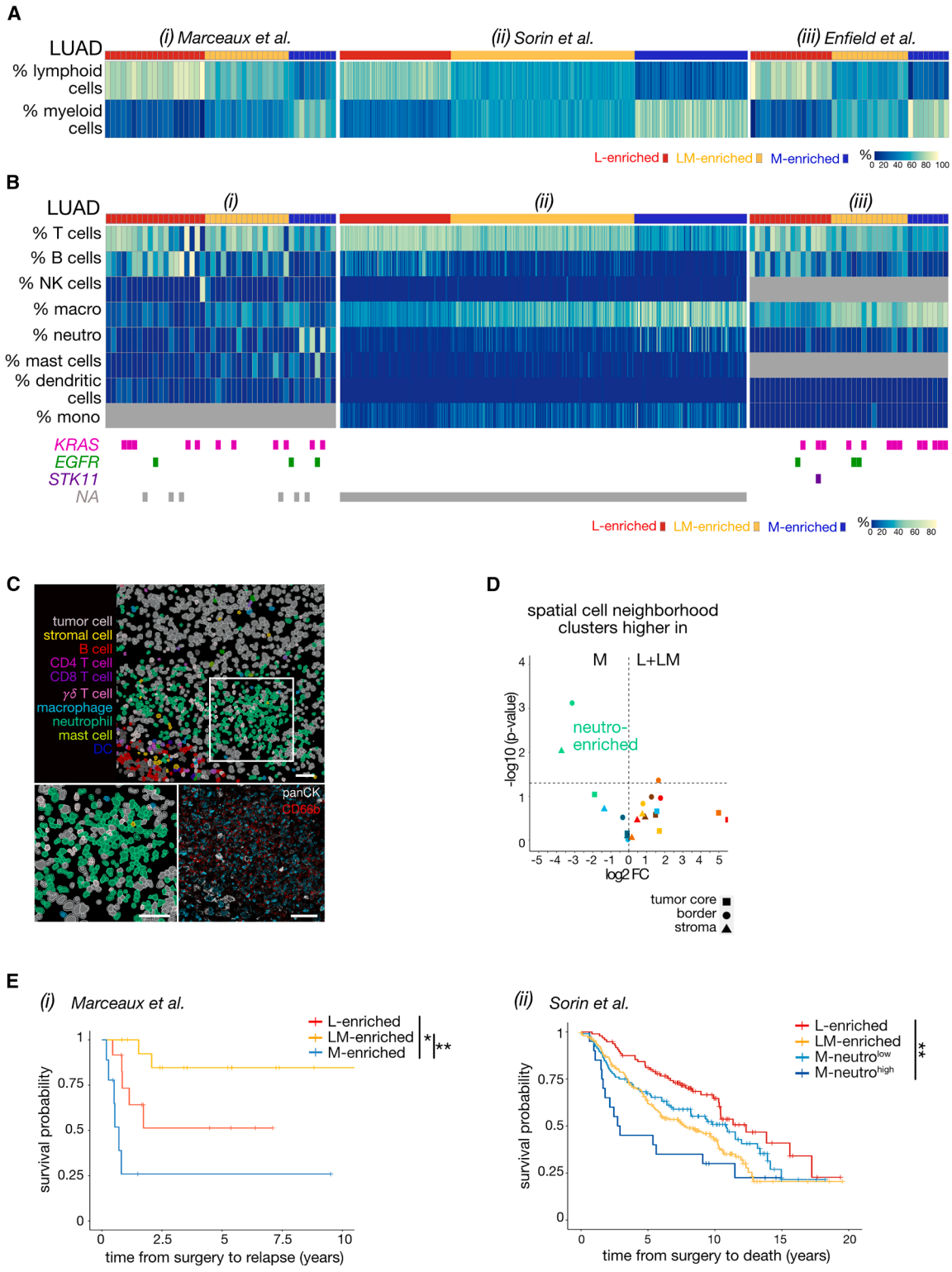

Figure 3. Enrichment for neutrophil clusters is associated with worst relapse-free survival in LUAD patients

(A) Heatmaps showing the proportion of lymphoid and myeloid cells in all immune cells in individual samples in LUAD in our cohort (i), Sorin et al. (ii), and Enfield et al. (iii). K-mean clustering stratified the TME in LUAD patients in the three cohorts in three immune subgroups (k = 3): lymphoid-enriched [L-enriched; $n = 19$ in (i); $n = 113$ in (ii); $n = 16$ in (iii)]; lymphoid-/myeloid-enriched [LM-enriched; $n = 16$ (i), $n = 118$ (ii), $n = 15$ (iii)]; or myeloid-enriched [M-enriched; $n = 9$ (i), $n = 115$ (ii), $n = 8$ (iii)].

(legend continued on next page)

between the two histological subtypes where dendritic cells were found enriched in LUAD stroma compared with LUSC, and mast cells were mostly present in the LUSC stroma compared with LUAD (Figure 2E). Together, these results point to a more myeloid-enriched microenvironment in LUSC compared with LUAD.

Analysis of immune cell neighborhoods (CN) revealed seven spatial clusters based on their immune composition, with neighborhoods of a single cell type (CN7: B cell, CN4: macrophages, and CN3: neutrophils), T cells (CN1 and 2 with higher prevalence of CD8 or CD4, respectively), lymphoid cells (CN6: B and T cells), and a mix of myeloid and T cells (CN5: T cells with macrophages and mast cells) (Figure 2F). Evaluating the presence of these clusters in LUAD and LUSC, we observed B-cell-enriched CN7 in the stroma and at the border of LUAD, whereas neutrophil-enriched CN3 was present in the stroma of LUSC (Figure 2G), indicating that these cell populations observed in each tumor subtypes infiltrate the tumor as cell communities and not as individual cells. Interestingly, the myeloid/T cell cluster was enriched in the stroma of LUSC compared with LUAD (Figure 2G).

Together, these analyses revealed key differences in the spatial organization and composition of the TME in LUSC and LUAD, highlighting essential immune cell communities characteristic of each tumor type.

Stratification of NSCLC according to myeloid and/or lymphoid cell infiltration is not associated with oncogenic driver mutations

We then investigated the heterogeneity of the TME between individual tumors in NSCLC. Quantification of the proportions of lymphoid and myeloid cells followed by unsupervised clustering resulted in the stratification of patients into two subgroups in LUSC (Figure S3A) and three subgroups in LUAD (Figures 3A and 3B). In LUSC, 15 tumors were characterized by a mix of lymphoid and myeloid cell infiltration (LM-enriched, 75%), with a TME rich in T and B cells with macrophages, mast cells, and dendritic cells. Five LUSC tumors were classified as myeloid-enriched with little lymphoid cell infiltration (M-enriched, 25%) (Figure S3A). In LUAD, most tumors had high lymphoid infiltration (79.5%) either alone (L-enriched, n = 19, 43%) or mixed with myeloid cell infiltration (LM-enriched, n = 16, 36%) (Figure 3A). Myeloid-enriched tumors only represented 20.5% of the LUAD samples (M-enriched, n = 9). We then analyzed two independent cohorts of NSCLC samples in which the tumor immune infiltrate was evaluated using Image Mass Cytometry,[13,28] a hi-plex mass-spectrometry-based imaging approach similar to the one we employed with the MIBIscope. Sorin et al. analyzed 416 LUAD samples with a 35-plex antibody panel to characterize cancer cells, stromal cells, and innate and adaptive immune cells,[13] while Enfield et al. analyzed 39 LUAD and 23 LUSC lesions with two distinct antibody panels to interrogate these cell types.[28] Consistent with our cohort, unsupervised clustering led to the stratification of LUAD tumors in L-, LM-, and M-enriched tumors (Figures 3A and 3B). In the two cohorts where genomic profiling was available (Marceaux et al. and Enfield et al.), $EGFR^{mut}$ or $KRAS^{mut}$ tumors were found in each subgroup: 2 $EGFR^{L858R}$ (5.7%) and 8 $KRAS^{mut}$ (22.9%) in the 35 L-enriched tumors; 2 $EGFR^{L858R}$ (6.5%) and 9 $KRAS^{mut}$ (29%) in the 31 LM-enriched; 2 $EGFR^{L858R}$ (11.8%) and 7 $KRAS^{mut}$ (41.2%) in the 17 M-enriched tumors (Figure 3B). $STK11^{mut}$ was only observed in one tumor in the L-enriched group. These results indicate that the type of immune infiltration in LUAD is not solely dictated by the presence of oncogenic driver mutations.

Neutrophil infiltration is associated with worse patient outcomes in LUAD

We then assessed differences between LUAD immune subgroups where we had the largest number of samples. L-enriched tumors had high T and B cell infiltration, although high B or T cell infiltration appeared to be mostly mutually exclusive (Figure 3B). LM-enriched tumors had lower B cell infiltration than L-enriched tumors and increased infiltration of macrophages (Figure 3B). We combined all patients with tumors harboring lymphoid infiltration (L-enriched and LM-enriched) as the LLM-enriched subgroup for further analysis. Only when quantifying immune cell infiltration in the individual tissue compartments did we observe that tumor cores infiltrated with B cells were significantly associated with long recurrence-free survival (RFS) (Figure S3B), consistent with previous work describing B cells infiltration as a predictor of long survival.[13]

In M-enriched tumors, the dominant populations were macrophages and neutrophils. Each myeloid cell subtype was located equally in the different tumor compartments, with the exception of dendritic cells that were more often found at the tumor border or in the stroma in LUAD (Figure S3C). The expression of functional markers of myeloid cells in LUAD was similar in each individual compartment (Figure S3D). A distinct feature of M-enriched tumors compared with LM-enriched tumors was a higher infiltration of neutrophils. Cell neighborhood analysis revealed that in all compartments of M-enriched tumors, neutrophils were present in clusters compared with L- and LM-enriched tumors (Figures 3C, 3D, and S3E). In our cohort, five out of the nine patients with an M-enriched LUAD had high neutrophils infiltration and an RFS of less than 7 months, significantly shorter than patients with L- and LM-enriched LUAD (median RFS 20.3 months and 64.9 months, respectively; Figures 3E and S3F). Of note, the long survivor with an M-enriched tumor had an $EGFR^{L858R}$ mutation characterized by a distinct TME compared with the other M-enriched tumors, with enrichment in mast cells and low levels of neutrophil

(B) Heatmaps showing the proportions of immune subpopulations for each patient in the three different immune subgroups. NA: not available.
(C) Representative image showing clustering of neutrophils in an LUAD tumor (MH1041). Scale bars: 50 μm.
(D) Volcano plots comparing the proportion of each CN cluster in between M− and L + LM-enriched LUAD samples. A horizontal dashed line indicates −log10(0.05), Wilcoxon test. n = 44 LUAD.
(E) Kaplan-Meier survival curve showing (i) relapse-free survival in the three groups of our LUAD patients (L-enriched, n = 19; LM-enriched, n = 16; and M-enriched, n = 9) and (ii) overall survival in the immune subgroups in Sorin et al. *p < 0.05, **p < 0.01 Cox proportional hazards regression model (Wald test). L-enriched, n = 113; LM-enriched, n = 118; M-Neutro^{low}-enriched, n = 95; M-Neutro^{high}-enriched, n = 20. See also Figures S3 and S4.

infiltration (Figure S3G). This observation is consistent with previous results showing that increased mast cells in the TME is associated with never-smoker patients and prolonged survival.[13] In Sorin et al.,[13] patients with M-enriched, high neutrophil-infiltrated tumors were found to have worse overall survival consistent with our cohort and previous studies[28] (Figure 3E). Neutrophil-enriched tumors also had worse survival in LUSC (Figure S3H).

We then compared the transcriptomic profile of panCK$^+$ tumor cells in M-enriched vs. LLM-enriched LUAD. We observed an upregulation of genes associated with type I IFN signaling in M-enriched tumors compared with LLM tumors (Figures S4A and S4B). Type I IFN signaling has also been shown to activate neutrophils with a pro-tumorigenic phenotype,[29–31] suggesting cancer cells in M-enriched tumor may support the recruitment and activation of myeloid cells.

Overall, these results demonstrate the inter-tumor heterogeneity in the TME of NSCLC, enabling the stratification of patients according to different types of immune infiltrate. We identified a subset of M-enriched tumors with a TME rich in neutrophils that was not observed when lymphoid cells were also present in the TME. Patients with these distinct neutrophil-enriched tumors had worse clinical outcomes, whereas LLM-enriched tumor with B cell infiltration specifically in the tumor core had better RFS.

CD14$^+$CD4$^+$ and CD14$^+$CD8$^+$ T cells are present in the microenvironment of LUAD and LUSC tumors

With the recent observation that myeloid cells can instruct T cells in hepatocarcinoma through the transfer of membrane material,[19] we evaluated whether CD14$^+$ T cells were also a feature of NSCLC. Quantification of CD14 expression in immune cell subsets in LUAD and LUSC tumors revealed that a subset of T cells expressed CD14 (Figures 4A, 4B, S5A, and S5B), the co-receptor for TLR-4-mediated lipopolysaccharide (LPS) recognition usually expressed by myeloid cells, indicating that these cells may be present in more organs than the liver, skin, and lymph node as described previously.[19] CD14$^+$ T cells were also detected in the Sorin and Enfield datasets (Figure S5C). In LUAD and LUSC, CD14$^+$CD4$^+$ T cells were present at a higher frequency than CD14$^+$CD8$^+$ T cells (Figures 4C and S5D), contrary to the results described in the liver where CD14$^+$CD8$^+$ T cells were predominant.[19] CD14$^+$ lymphoid cells represented 8.5%–15% of CD8$^+$, Tregs, and CD4$^+$ T cells in LUAD (Figure 4C). As a proportion of their parent population, CD14$^+$CD4$^+$ T cells were present equally in the tumor core, at the border or stroma (Figure S5E). The presence of CD14$^+$ T cells in NSCLC was further confirmed by flow cytometry analysis of fresh human lung tumors (Figures 4D and S5F). Image cytometry and Hoechst 33342 analysis confirmed that CD14$^+$CD4$^+$ T cells were single cells and not a complex of monocytes/T cells as detected in the blood[32,33] (Figures 4E and S5G).

To evaluate the process by which the co-expression of a myeloid marker and T cell markers could occur, we performed trogocytosis experiments where membrane-labelled T cells (CD3$^+$TCR$\alpha\beta^+$) were incubated with HLA-DR$^+$ cells or vice-versa in which membrane-labelled HLA-DR$^+$ cells were incubated with CD3$^+$TCR$\alpha\beta^+$ cells (Figure 4F). Transfer of membrane only occurred from HLA-DR$^+$ cells to T cells and was most predominant in CD4$^+$ T cells (Figures 4G and 4H), indicating that only T cells can take up membrane from myeloid cells.

Overall, these data reveal the existence of a discrete subset of CD4$^+$ T cells harboring the myeloid marker CD14 in NSCLC and that this phenomenon may be mediated by T cell trogocytosis from HLA-DR$^+$ myeloid cells.

CD14$^+$ T cells are not detected in healthy lungs and are located within myeloid cell neighborhoods in LUAD

We then assessed whether CD14$^+$CD4$^+$ T cells were a unique feature of tumors or were also present in the non-malignant or healthy lung tissues. CD14$^+$CD4$^+$ T cells were observed in the non-malignant lung of lung cancer patients in proportions similar to what was observed in matched tumors (Figure 5A). However, CD14$^+$CD4$^+$ T cells were not detected in four lung samples obtained from healthy donors (Figure 5A), indicating that CD14$^+$CD4$^+$ T cells may be induced in an oncogenic context. Consistently, the vast majority of CD14$^+$CD4$^+$ T cells expressed CD39 (Figure 5B), a surrogate marker of tumor-specific lymphocytes, whereas only a subset of CD14$^-$CD4$^+$ T cells expressed CD39. While CD39 expression on T cells is an indirect marker of tumor-antigen specificity,[34–36] these data suggest that CD14$^+$CD4$^+$ T cells may be enriched for tumor-specific T cell clones. To assess the clonality of CD14$^+$ T cells, we compared the T cell receptor beta chain (TCRβ) repertoire of CD14$^+$CD4$^+$ and CD14$^-$CD4$^+$ T cells by TCR sequencing of sorted cell subsets. Sequencing results showed an expansion of some TCRβ clones in CD14$^+$ cells compared to CD14$^-$ cells (Figure S6A), indicating CD14$^+$CD4$^+$ T cells may be an expanded population of T cell clones present in tumors, although the tumor specificity of these clones cannot be concluded.

To better understand the context in which CD14$^+$CD4$^+$ T cells arise, we investigated whether the presence of CD14$^+$CD4$^+$ T cells was correlated with abundance and spatial organization of other immune cell types. For this analysis, we exploited the Sorin et al. dataset,[13] given the large number of samples available. Proportions of CD14$^+$CD4$^+$ T cells were correlated with the presence of classical and intermediate monocytes, two populations of CD14-expressing immune cells (Figure 5C), as well as the proportion of CD14$^+$CD8$^+$ T cells (Figure S6B). However, an inverse correlation was observed with CD14$^-$CD4$^+$ and CD8$^+$ T cells (Figure S6B). The proportion of CD14$^+$CD4$^+$ T cells was not correlated with the presence of other lymphoid cell types, including immunosuppressive Tregs, natural killer (NK), or B cells (Figures 5C and S6B), nor with the presence of neutrophils, mast cells, or dendritic cells (Figure S6B).

To define the cellular niche in which CD14$^+$CD4$^+$ T cells may be found, we first quantified cell-cell distances to CD14$^+$CD4$^+$ T cells and CD14$^-$CD4$^+$ T cells within each sample. These analyses revealed that CD14$^+$CD4$^+$ T cells were in close proximity to myeloid cells and other CD14-expressing cells, whereas CD14$^-$CD4$^+$ T cells were closer to lymphoid cells (Figures 5D and 5E). Analysis of cell-cell interaction shows that homotypic interactions, where identical cell types interact with each other, is a clear feature of the NSCLC TME (Figure 5F). T cells in general,

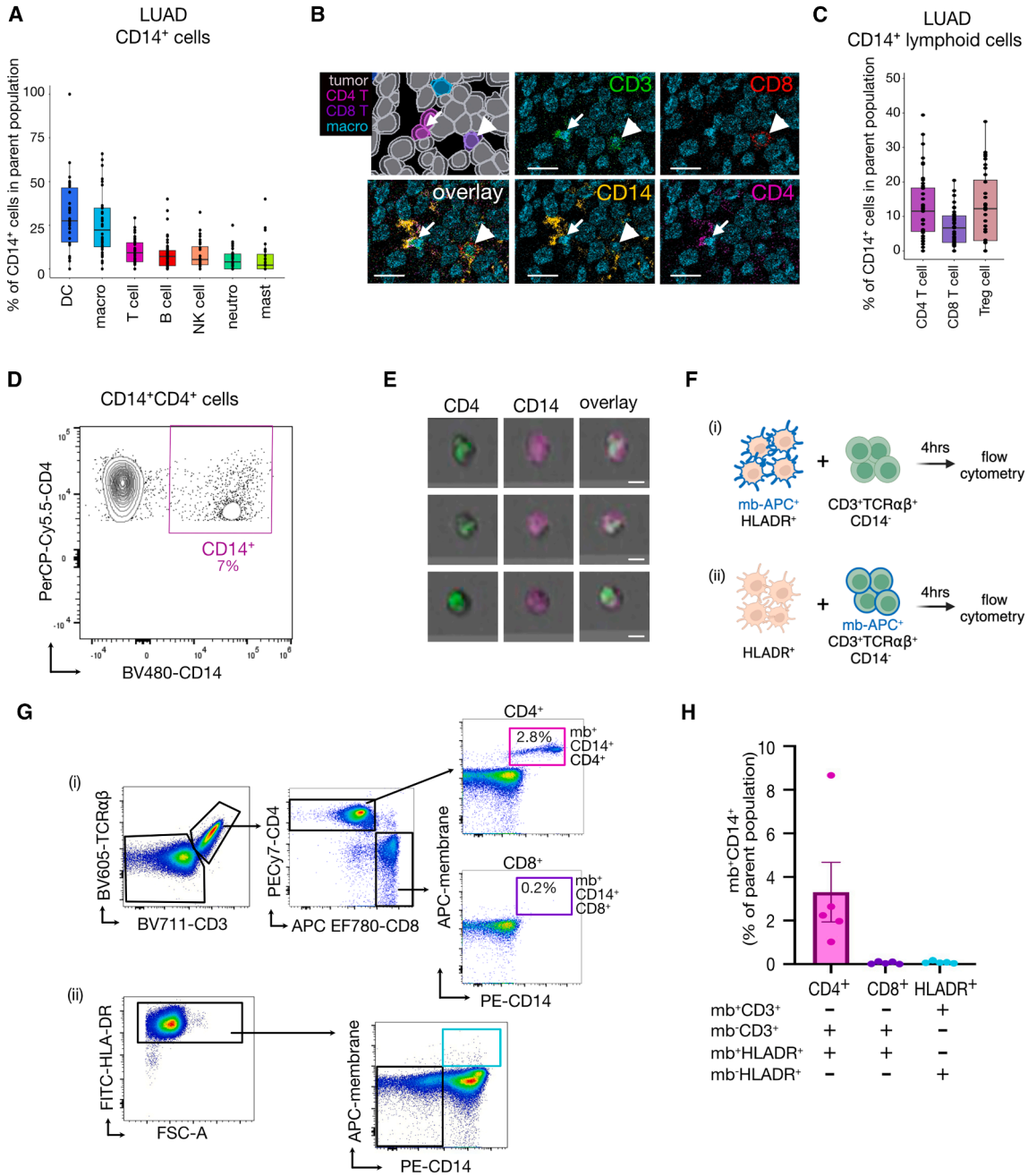

Figure 4. Myeloid-instructed CD14$^+$ T cells infiltrate tumors in non-small cell lung cancer

(A) Proportion of immune cell types expressing CD14 in LUAD as determined by MIBI. Data show median ± SD. *n* = 44 LUAD.

(B) Representative MIBI images showing the expression of indicated markers in a representative LUAD tumor (AH0353). Arrow and arrowhead show CD14 expression in CD3$^+$CD4$^+$ and CD3$^+$CD8$^+$ T cells, respectively.

(C) Boxplot showing the proportion of cells expressing CD14 in lymphoid cells in LUAD as determined by MIBI. Data show median ± SD. *n* = 42 LUAD. Scale bars: 10 μm. (D) Flow cytometry plot showing CD14 expression in CD4$^+$ T cells gated on CD45$^+$CD3$^+$ cells in an LUAD sample (MH0069).

(E) Representative image cytometry images showing the expression of CD14 and CD4 on CD45$^+$CD3$^+$CD4$^+$ cells. *n* = 2. Scale bars: 5 μm. (F) Schematic of trogocytosis assay.

(G) Representative flow cytometry plots showing the membrane transfer from HLADR$^+$ cells to CD4$^+$ T cells (i) and the absence of transfer of membrane from T cells to HLA-DR$^+$ cells (ii).

(H) Percentage of membrane$^+$CD14$^+$ in CD4$^+$, CD8$^+$ T cells, and HLADR$^+$ cells. Data show mean ± SEM (*n* = 5 biological replicates). See also Figure S5.

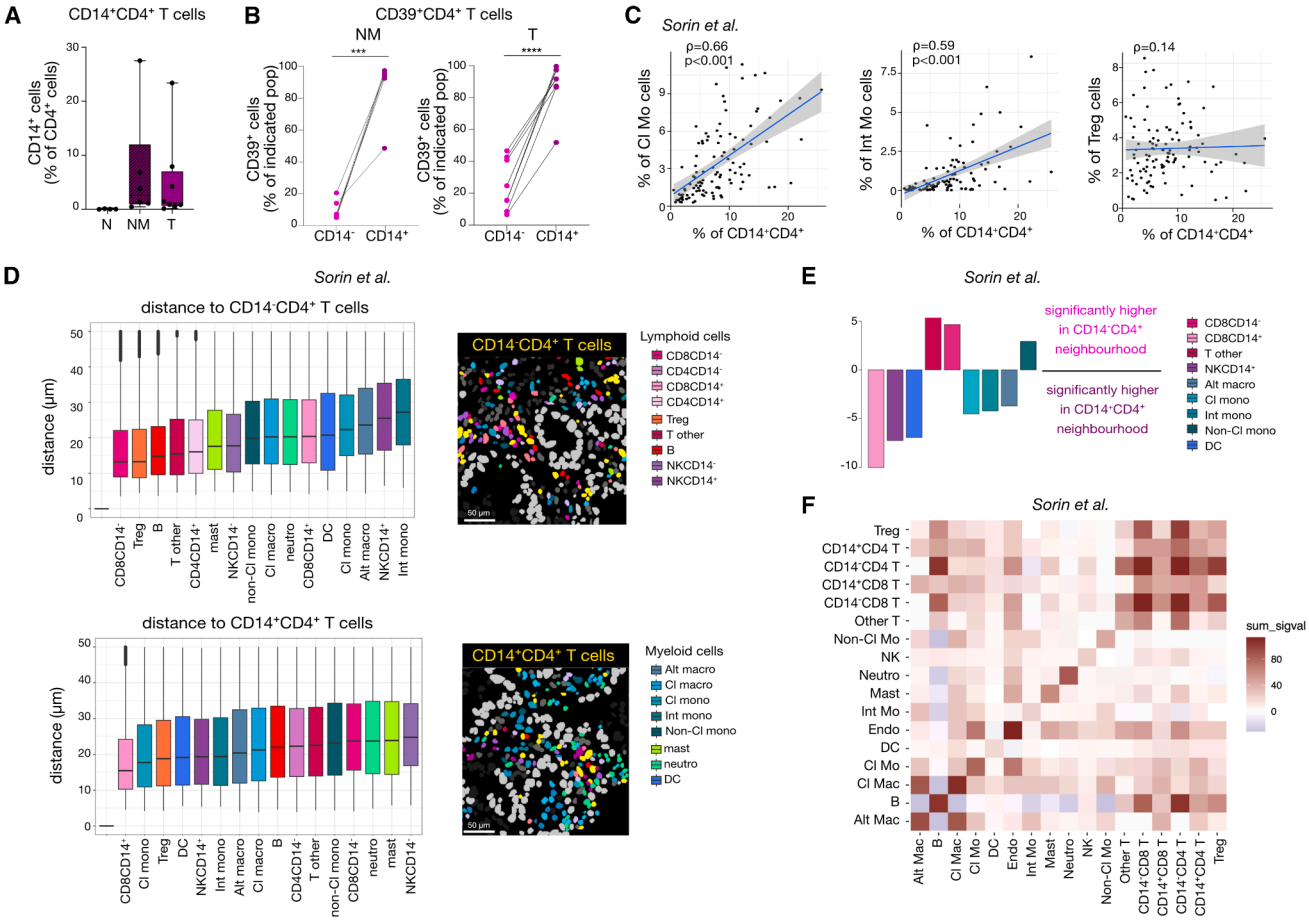

Figure 5. Myeloid-instructed CD14⁺CD4⁺ T cells reside in a myeloid-enriched microenvironment

(A) Flow cytometry quantification of percentage of CD14⁺CD4⁺ T cells in normal lung (N). Data show median ± SD (n = 4), non-malignant lung (NM) (n = 6), and tumor (T) (n = 8).

(B) Proportion of CD14⁺CD4⁺ and CD14⁻CD4⁺ T cells expressing CD39 in non-malignant lung tissues (NM) (n = 5) and tumor tissues (T) (n = 7). n = 4 LUAD, n = 3 LUSC, and n = 1 carcinoid. ***$p < 0.001$; **$p < 0.01$; *$p < 0.05$; paired t test between CD14⁺ and CD14⁻ T cell subsets.

(C) Correlation plots between the proportion of CD14⁺CD4⁺ T cells and indicated cell types in Sorin et al. L-enriched subgroup. Spearman rank correlation. n = 113 LUAD.

(D) Distance between indicated cell type and CD14⁻CD4⁺ T cells (top left) or CD14⁺CD4⁺ T cells (bottom left) within 50 µm radius in Sorin et al. L-enriched subgroup (n = 112 LUAD). Data show median ± IQR (interquartile range). Right shows representative images of segmented cells in the microenvironment around CD14⁻CD4⁺ T cells (yellow, top) and CD14⁺CD4⁺ T cells (yellow, bottom). Scale bar: 50 µm.

(E) Output of Propeller analysis showing cell-type proportion significantly higher in CD14⁻CD4⁺ T cells and CD14⁺CD4⁺ T cells neighborhood in Sorin et al. L-enriched subgroup (n = 112 LUAD). The y axis shows t-statistics after filtering by FDR<0.05.

(F) Heatmap representative of cell-cell interaction compared to random permutations distribution in Sorin et al. cohort L-enriched immune subgroup (n = 113 LUAD). See also Figure S6.

including Treg, had more cell interactions between themselves than any other cell types, with the CD8⁺ and CD4⁺ T cell interactions being the strongest after homotypic interactions. CD14⁻CD4⁺ T cells interacted more with CD14⁻CD8⁺ T cells than CD14⁺ T cells, while CD14⁺CD4⁺ T cells interacted more with CD14⁺ T cells and myeloid cells than CD14⁻ T cells. Among their myeloid cell interactions, CD14⁺CD4⁺ T cells showed attraction toward monocytes and macrophages, but little attraction to neutrophils. B cells interacted with other lymphoid subsets but showed repulsion with myeloid cell subsets including macrophages, monocytes, and neutrophils (Figure 5F).

Overall, these spatial analyses indicate that CD14⁺CD4⁺ T cells evolve in a myeloid-enriched niche that favors interactions with other CD14-expressing T cells, macrophages, and monocytes.

CD14⁺CD4⁺ T cells represent a distinct, myeloid-instructed T cell population associated with poor prognosis and TNF-α-driven signaling

Trogocytosis is a dynamic process that involves the transfer of plasma membrane and its associated cytosol between two cell types, resulting in changes in the functional properties of

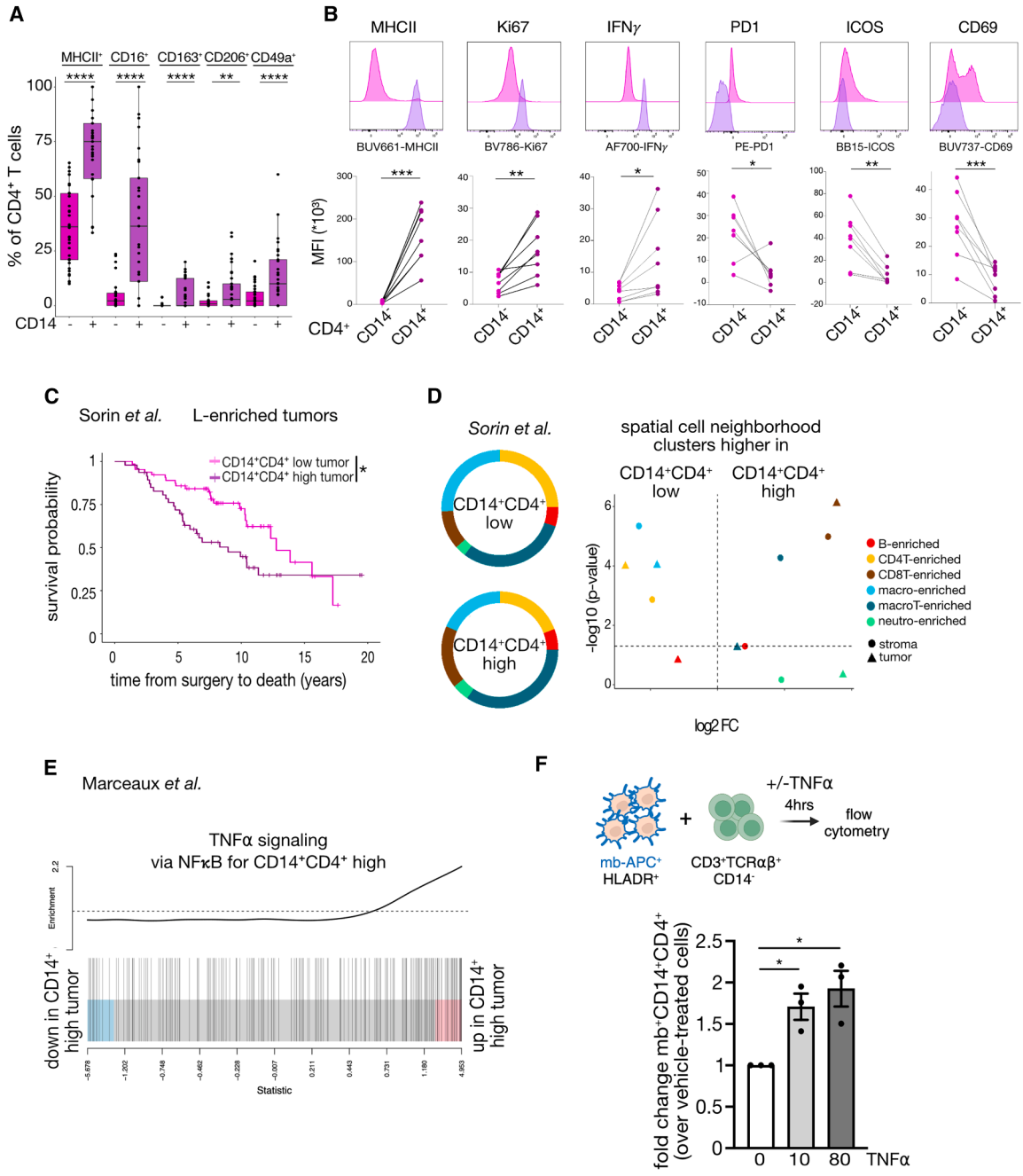

Figure 6. High infiltration of CD14$^+$CD4$^+$ T cells is associated with poor survival and high TNF-α signaling

(A) Expression of indicated markers in CD14$^+$CD4$^+$ and CD14$^-$CD4$^+$ T cells as determined by MIBI. ***$p < 0.001$; **;$p < 0.01$; *$p < 0.05$; paired *t* test. Data show median ±SD. $n = 42$ LUAD.

(B) Mean fluorescence intensity (MFI) of myeloid (MHC class II) and functional markers in CD14$^+$CD4$^+$ and CD14$^-$CD4$^+$ T cells in NSCLC as assessed by flow cytometry. Cells were gated on Live CD45$^+$CD3$^+$CD4$^+$CD14$^{+/-}$ cells. $n = 4$ LUAD, $n = 3$ LUSC, and $n = 1$ carcinoid. **$p < 0.01$; *$p < 0.05$; paired *t* test between CD14$^+$ and CD14$^-$ T cell subsets.

(C) Kaplan-Meier survival curve showing overall survival of L-enriched tumors in Sorin et al. with low ($n = 64$) or high ($n = 47$) CD14$^+$CD4$^+$ T cells infiltration in the tumor. *$p < 0.05$; Cox proportional hazards regression model (Wald test).

(D) Spatial neighborhood analysis of immune cells in Sorin et al. Left: pie charts of proportion of cell neighborhood (CN) clusters in patients with low (top) or high (bottom) CD14$^+$CD4$^+$ T cells infiltration in the tumor core. Right: volcano plots comparing the proportion of each CN clusters between patients with low ($n = 64$) or high ($n = 47$) CD14$^+$CD4$^+$ T cells infiltration. Wilcoxon test.

(legend continued on next page)

the recipient cell.[37] Functional characterization of $CD14^+CD4^+$ T cells using spatial proteomics data revealed $CD14^+CD4^+$ T cells express other prototypic markers of myeloid cells (MHC-II, CD16, CD163, and CD206) and a marker of tissue residency (CD49a[38]) (Figure 6A) but lower expression of CD103 (Figure S7A). Flow cytometry data further showed that $CD14^+CD4^+$ T cells have a distinct activation phenotype to their $CD14^-$ counterparts, exhibiting elevated expression of Ki67, IFN-γ, and OX40 but low expression of canonical co-activation (ICOS) and exhaustion marker (PD1) or T cell activation (CD69) (Figures 6B and S7B). While this profile does not align with classical effector or helper T cell subsets, it may reflect a tumor-adapted state associated with an inflammatory environment.

We then examined the clinical relevance of $CD14^+CD4^+$ T cells infiltration in tumors. High infiltration of $CD14^+CD4^+$ T cells in L-enriched tumors (Sorin et al.; $n = 111$) was significantly associated with poorer overall survival (median survival 9 years vs. 12.8 years in $CD14^+CD4^+$ high vs. low tumors, respectively) (Figure 6C). However, this association was not observed in the LM-enriched or M-enriched subgroups (Figure S7C). The majority of the tumors in this cohort are stage 1–2 tumors (88%, corresponding to 94%, 88%, and 82% of L-, LM-, and M-enriched tumors, respectively). High infiltration of $CD14^+CD4^+$ T cells was associated with survival in stage 1–2 tumors but not in stage 3–4 tumors (Figure S7C). Spatial neighborhoods analysis showed that tumors with high $CD14^+CD4^+$ T cell infiltration had a distinct cellular microenvironment, enriched in macrophage/T cell clusters (Figures 6D and S7D), consistent with the observation that $CD14^+CD4^+$ T cells reside in myeloid-rich niches (Figures 5D, 5E, and 5F). Evaluation of the demographics and clinical characteristics of the patients in $CD14^+CD4^+$ low and high tumors show similar age, gender, BMI, smoking status, and disease stages between the two groups. Histological patterns were slightly different with more acinar patterns in $CD14^+CD4^+$ low tumors and more solid patterns in $CD14^+CD4^+$ high tumors (Table S3).

To evaluate whether the infiltration of $CD14^+CD4^+$ T cells could be associated with a specific tumor cell phenotype, we compared the transcriptional profiles of tumor cells in $CD14^+CD4^+$-high tumors and $CD14^+CD4^+$-low tumors. KEGG pathway enrichment analysis identified cytokine signaling pathways upregulated in tumors with high $CD14^+CD4^+$ T cells infiltration, indicative of an inflammatory microenvironment, while metabolic pathways were downregulated in tumors with high infiltration of $CD14^+CD4^+$ T cells (Figure S7E). Specifically, the TNF-α signaling pathway was enriched in tumors with high infiltration of $CD14^+CD4^+$ T cells (Figure 6E). Given the known immunosuppressive effect of TNF-α on the tumor microenvironment,[20] we evaluated whether it could alter the properties of $CD4^+$ T cells by enhancing T cell trogocytosis from myeloid cells. Trogocytosis assay showed that TNF-α increased the capture of membrane components by $CD4^+$ T cells from $HLA\text{-}DR^+$ cells by 1.7- to 1.9-fold (Figure 6F) compared to vehicle-treated cells. These results show that TNF-α present in the TME may enhance $CD4^+$ T cell trogocytosis, enhancing the formation of myeloid-instructed T cells, a mechanism that may contribute to TNF-α-mediated pro-tumorigenic properties.

DISCUSSION

Advances in cancer immunotherapy have greatly improved outcomes for lung cancer patients. However, not all patients respond to treatment,[1,2] indicating that alternative approaches to increase anti-cancer immunity are urgently needed. In-depth characterization of the composition and spatial organization of individual immune cells in the TME, and the signals that regulate them, is essential in identifying pathways to deplete pro-tumorigenic cells to bolster anti-tumor immunity.

In situ analysis of individual cells in solid tumors presents a clear advantage over single-cell analysis of dissociated tissue. Notably, the architecture of the tissue is preserved, adding to the depth of knowledge on the role of cell communities in the anti-tumor immune response. In addition, this approach also avoids disproportionate recovery of different cell types, which is known to occur after tissue disruption.[39] Our comparison of the *in situ* TME in different histological subtypes of NSCLC revealed similarities and distinctions in the composition and organization of the TME of LUAD and LUSC. As described by others,[11,23] we observed a higher proportion of immune cells in the stroma and at the tumor border than in the tumor core. However, macrophages and $CD8^+$ T cells were more predominant in the tumor core than the border and the stroma in both LUAD and LUSC. Myeloid cells were always observed in LUSC, whereas nearly half of the LUAD samples had little myeloid cell infiltration. Cell neighborhood analysis showed that immune cells were mostly present as clusters of single-cell types or cells from similar lineages. Mixed myeloid and T cell cellular neighborhoods were a distinctive feature of the LUSC TME, whereas B cell clusters were only observed in LUAD and associated with better survival in LUAD, as described by Sorin et al.[13]

By profiling the TME in NSCLC, we were able to stratify LUAD and LUSC in different immune categories. M-enriched tumors had a distinct myeloid cell infiltration compared with LM-enriched tumors. While neutrophils were the predominant myeloid cell type in M-enriched tumors, macrophages constituted the bulk of the myeloid infiltrate in LM-enriched tumors. Neutrophils have a multi-faceted role in cancer[29,40] but have often been associated with worse clinical outcomes in solid tumors, facilitating tumor cell extravasation and metastasis.[41–43] A high neutrophil-to-lymphocyte ratio has been associated with worse overall survival in many solid malignancies, including lung cancer,[16,28] consistent with our observation that tumors with clusters of neutrophils had worse survival.

Focusing on tumors with lymphoid cell infiltration, we observed that a subset of $CD4^+$ and $CD8^+$ T cells expressed

(E) Enrichment for TNF-α signaling pathway in tumors with high $CD14^+CD4^+$ T cells infiltration.
(F) Schematic of trogocytosis experiment with or without TNF-α (top). Fold change in membrane-labelled $CD14^+CD4^+$ T cells after treatment with TNF-α (bottom). Data show mean ± SEM ($n = 3$ biological replicates). See also Figure S7 and Table S3.

the myeloid cell marker CD14, similar to the $CD14^+CD8^+$ and $CD14^+CD4^+$ T cells described in human liver.[19] Detailed analysis by Pallett et al. demonstrated that $CD14^+$ T cells were myeloid-instructed T cells, in which $CD8^+$ T cells acquired cellular myeloid materials from $CD14^+$ myeloid cells in a contact-dependent manner. Exposure to bacterial LPS promoted the transfer of myeloid materials to T cells, with the presence of bacteria reshaping the local immunity and inducing the expansion of $CD14^+CD8^+$ T cells.[19] The lung is host to a diverse range of commensal bacteria,[44] and increased bacterial colonization is observed in lung tumors.[45–48] Further studies would be required to investigate the relationship between $CD14^+$ T cells, the tumor microbiota, and the implication for response to immunotherapy.

Importantly, we observed that patients with L-enriched tumors with a high infiltration of $CD14^+$-expressing $CD4^+$ T cells had poor survival, pointing to $CD14^+CD4^+$ T cells being unable to support anti-tumor immunity. T cell trogocytosis is a known phenomenon that has been shown to involve antigen-presenting cells[49] or B cells,[50] leading to the transfer of a number of immune regulatory molecules such as HLA-G, PDL1, and OX40L that can reduce anti-tumor immunity. We demonstrated that $CD14^+CD4^+$ T cells can form through trogocytosis and that in NSCLC, these myeloid-instructed $CD14^+CD4^+$ T cells were more frequent than $CD14^+CD8^+$ T cells. $CD14^+CD4^+$ T cells had unusual phenotype-expressing markers of T cell activation (IFN-γ, Ki67, and CD39) but low levels of PD1, ICOS, and CD69. We found that TNF-α increased $CD4^+$ T cell trogocytosis from $HLA\text{-}DR^+$ myeloid cells. TNF-α can exert both tumor-promoting and tumor-suppressing activities,[20] but combination drug studies show that inhibition of TNF-α in combination with immune checkpoint inhibitors increases treatment response,[51] suggesting a predominant role for TNF-α in promoting tumor growth. TNF-α exerts its pro-tumorigenic activity in multiple ways, including the recruitment of myeloid and myeloid-derived suppressor cells to the TME and maintaining regulatory T cell function.[20,52] Here, we identify a possible mechanism by which TNF-α exerts its pro-tumor activity, by facilitating T cell trogocytosis, thereby altering their anti-tumor properties. Trogocytosis has been described as an antigen-specific, TCR-affinity-dependent process.[53,54] TNF-α may increase T cell-antigen-presenting cell interaction, promoting T cells trogocytosis. Future work would be needed to evaluate whether $CD14^+CD4^+$ T cells are depleted in tumors treated with TNF-α inhibitors, such as infliximab, and determine the relative contribution of this process to the overall pro-tumorigenic activities of TNF-α.

Overall, our study demonstrates the importance of undertaking a comprehensive analysis of the tumor ecosystem with high-plex *in situ* molecular approaches to uncover novel cell types and decipher spatial relationships between immune and tumor cells. Our study revealed myeloid-instructed T cells in the TME may participate in tumor immune escape. Targeting the recruitment or formation of myeloid-instructed T cells to the tumor core, such as with the TNF-α inhibitor infliximab, may provide novel therapeutic avenues for lung cancer patients.

Limitations of the study

This analysis was well powered to evaluate stage 1–2 treatment-naïve LUAD patients, but a relatively small number of stage 3–4 samples and LUSC samples limit the generalizability of the findings to all NSCLC. While the application of spatial multi-omics enabled the identification of novel immune cell states within the preserved tumor architecture, functional validation of these mechanisms was primarily undertaken *in vitro*, and their *in vivo* significance remains to be determined. Moreover, the precise role of $CD14^+CD4^+$ T cells in shaping anti-tumor immunity is incompletely defined, and potential interactions with other modulators of the tumor microenvironment, such as the microbiota or immune checkpoint blockade, were not assessed. Finally, although TNF-α was implicated as a driver of trogocytosis and myeloid-instructed T cell formation, the relative contribution of this pathway compared with other immunoregulatory mechanisms warrants further investigation. From a technical perspective, the resolution and marker selection for the spatial proteomic analyses constrain the detection of additional immune subsets or functional states. Tissue sampling bias cannot be excluded.

RESOURCE AVAILABILITY

Lead contact

Requests for further information and resources should be directed to and will be fulfilled by the lead contact, Marie-Liesse Asselin-Labat (labat@wehi.edu.au).

Materials availability

This study did not generate any custom materials.

Data and code availability

- GeoMx and Spatial Proteomic data (image mass cytometry with MIBI) have been deposited on Zenodo and are publicly available at https://doi.org/10.5281/zenodo.17051520.
- Codes are available at https://github.com/WEHI-labatlab/lung-mibi-cd14cd4.
- Any additional information required to reanalyze the data reported in this paper is available from the lead contact upon request.

ACKNOWLEDGMENTS

We thank WEHI facilities including Histology (Emma Pan and Ellen Tsui), Flow cytometry (Simon Monard), and the Research Computing Platform (Julie Iskander, Michael McKay) for expert advice. We are grateful to the Victorian Cancer Biobank and all lung cancer patients who participated in this study. Real-time images of the cells were captured using a BD FACSDiscover S8 Cell Sorter located at BD Melbourne, Australia, with the assistance of the BD Biosciences ANZ applications team. C.M. was supported by a bequest from the late Margaret Anne Ireland and funds from the Harry Secomb Trust-Perpetual Impact. B.P. is supported by an NHMRC Investigator grant (GNT1175653). The MIBI studies were supported by the Australian Cancer Research Foundation Program for Resolving Cancer Complexity and Therapeutic Resistance and the Kinghorn Foundation Spatial Omics Data Analytics (SODA) Hub. The Victorian Cancer Biobank is supported by the Victorian Government through the Victorian Cancer Agency, a business unit of the Department of Health. This work is supported by an NHMRC Ideas grant (GNT1182155), a Lyn Williams research grant, Jenny Tatchell research grant, and by funds from the Operational Infrastructure Support Program provided by the Victorian Government and NHMRC IRIISS grant (Independent Research Institutes Infrastructure Support Scheme).

AUTHOR CONTRIBUTIONS

Conceptualization, C.M. and M.-L.A.-L. Data curation, C.M., J.H., and M.C. Formal analysis, C.M., I.T., K.Y., V.G., N.T.R., E.Y., L.R., T.P.S., and B.P.

Funding acquisition, M.-L.A.-L. and B.P. Methodology, C.M., R.J., M.L., L.C., and D.B. Resources, P.A. and K.L.R. Supervision, M.-L.A.-L., B.P., and K.L.R. Validation, R.J., M.L., L.C., and D.B. Writing—original draft, C.M. and I.T. Writing—review and editing, M.-L.A.-L. and B.P.

DECLARATION OF INTERESTS

M.-L.A.-L. serves as a scientific advisor for Esobiotec.

STAR★METHODS

Detailed methods are provided in the online version of this paper and include the following:

- KEY RESOURCES TABLE
- EXPERIMENTAL MODEL AND STUDY PARTICIPANT DETAILS
  - Human samples
  - Non-small cell lung cancer imaging datasets
- METHOD DETAILS
  - Human lung and tumor tissue dissociation
  - Flow cytometry
  - Image cytometry
  - Trogocytosis
  - TCR sequencing
  - Oncogenic driver mutation sequencing
  - GeoMx data collection
  - Validation of 38-plex antibody panel for MIBI
  - Slide staining and scanning on MIBI
- QUANTIFICATION AND STATISTICAL ANALYSIS
  - Single-cell segmentation and classification on MIBI data
  - Tissue classifier and immune subgroup classification
  - Cell neighborhood clustering of immune cells
  - Sorin et al. and Enfield et al. analysis
  - GeoMx data analysis
  - Statistical analysis

SUPPLEMENTAL INFORMATION

Supplemental information can be found online at https://doi.org/10.1016/j.xcrm.2026.102593.

Received: March 12, 2024
Revised: September 8, 2025
Accepted: January 8, 2026
Published: February 9, 2026

REFERENCES

1. Langer, C.J., Gadgeel, S.M., Borghaei, H., Papadimitrakopoulou, V.A., Patnaik, A., Powell, S.F., Gentzler, R.D., Martins, R.G., Stevenson, J.P., Jalal, S.I., et al. (2016). Carboplatin and pemetrexed with or without pembrolizumab for advanced, non-squamous non-small-cell lung cancer: a randomised, phase 2 cohort of the open-label KEYNOTE-021 study. Lancet Oncol. *17*, 1497–1508. https://doi.org/10.1016/s1470-2045(16)30498-3.
2. Gandhi, L., Rodríguez-Abreu, D., Gadgeel, S., Esteban, E., Felip, E., De Angelis, F., Domine, M., Clingan, P., Hochmair, M.J., Powell, S.F., et al. (2018). Pembrolizumab plus Chemotherapy in Metastatic Non–Small-Cell Lung Cancer. N. Engl. J. Med. *378*, 2078–2092. https://doi.org/10.1056/nejmoa1801005.
3. Rizvi, H., Sanchez-Vega, F., La, K., Chatila, W., Jonsson, P., Halpenny, D., Plodkowski, A., Long, N., Sauter, J.L., Rekhtman, N., et al. (2018). Molecular Determinants of Response to Anti–Programmed Cell Death (PD)-1 and Anti–Programmed Death-Ligand 1 (PD-L1) Blockade in Patients With Non–Small-Cell Lung Cancer Profiled With Targeted Next-Generation Sequencing. J. Clin. Orthod. *36*, 633–641. https://doi.org/10.1200/jco.2017.75.3384.
4. Hellmann, M.D., Nathanson, T., Rizvi, H., Creelan, B.C., Sanchez-Vega, F., Ahuja, A., Ni, A., Novik, J.B., Mangarin, L.M.B., Abu-Akeel, M., et al. (2018). Genomic Features of Response to Combination Immunotherapy in Patients with Advanced Non- Small-Cell Lung Cancer. Cancer Cell *33*, 843–852.e4. https://doi.org/10.1016/j.ccell.2018.03.018.
5. Weeden, C.E., Gayevskiy, V., Marceaux, C., Batey, D., Tan, T., Yokote, K., Ribera, N.T., Clatch, A., Christo, S., Teh, C.E., et al. (2023). Early immune pressure initiated by tissue-resident memory T cells sculpts tumor evolution in non-small cell lung cancer. Cancer Cell *41*, 837–852.e6. https://doi.org/10.1016/j.ccell.2023.03.019.
6. Angelova, M., Mlecnik, B., Vasaturo, A., Bindea, G., Fredriksen, T., Lafontaine, L., Buttard, B., Morgand, E., Bruni, D., Jouret-Mourin, A., et al. (2018). Evolution of Metastases in Space and Time under Immune Selection. Cell *175*, 751–765.e16. https://doi.org/10.1016/j.cell.2018.09.018.
7. Kirchhammer, N., Trefny, M.P., Auf der Maur, P., Läubli, H., and Zippelius, A. (2022). Combination cancer immunotherapies: Emerging treatment strategies adapted to the tumor microenvironment. Sci. Transl. Med. *14*, eabo3605. https://doi.org/10.1126/scitranslmed.abo3605.
8. Bruni, D., Angell, H.K., and Galon, J. (2020). The immune contexture and Immunoscore in cancer prognosis and therapeutic efficacy. Nat. Rev. Cancer *20*, 662–680. https://doi.org/10.1038/s41568-020-0285-7.
9. Lambrechts, D., Wauters, E., Boeckx, B., Aibar, S., Nittner, D., Burton, O., Bassez, A., Decaluwé, H., Pircher, A., Van den Eynde, K., et al. (2018). Phenotype molding of stromal cells in the lung tumor microenvironment. Nat. Med. *24*, 1277–1289. https://doi.org/10.1038/s41591-018-0096-5.
10. Guo, X., Zhang, Y., Zheng, L., Zheng, C., Song, J., Zhang, Q., Kang, B., Liu, Z., Jin, L., Xing, R., et al. (2018). Global characterization of T cells in non-small-cell lung cancer by single-cell sequencing. Nat. Med. *24*, 978–985. https://doi.org/10.1038/s41591-018-0045-3.
11. Lavin, Y., Kobayashi, S., Leader, A., Amir, E.A.D., Elefant, N., Bigenwald, C., Remark, R., Sweeney, R., Becker, C.D., Levine, J.H., et al. (2017). Innate Immune Landscape in Early Lung Adenocarcinoma by Paired Single-Cell Analyses. Cell *169*, 750–765.e17. https://doi.org/10.1016/j.cell.2017.04.014.
12. Leader, A.M., Grout, J.A., Maier, B.B., Nabet, B.Y., Park, M.D., Tabachnikova, A., Chang, C., Walker, L., Lansky, A., Le Berichel, J., et al. (2021). Single-cell analysis of human non-small cell lung cancer lesions refines tumor classification and patient stratification. Cancer Cell *39*, 1594–1609.e12. https://doi.org/10.1016/j.ccell.2021.10.009.
13. Sorin, M., Rezanejad, M., Karimi, E., Fiset, B., Desharnais, L., Perus, L.J.M., Milette, S., Yu, M.W., Maritan, S.M., Doré, S., et al. (2023). Single-cell spatial landscapes of the lung tumour immune microenvironment. Nature *614*, 548–554. https://doi.org/10.1038/s41586-022-05672-3.
14. Desharnais, L., Sorin, M., Rezanejad, M., Liu, B., Karimi, E., Atallah, A., Swaby, A.M., Yu, M.W., Doré, S., Hartner, S., et al. (2025). Spatially mapping the tumour immune microenvironments of non-small cell lung cancer. Nat. Commun. *16*, 1345. https://doi.org/10.1038/s41467-025-56546-x.
15. Casanova-Acebes, M., Dalla, E., Leader, A.M., LeBerichel, J., Nikolic, J., Morales, B.M., Brown, M., Chang, C., Troncoso, L., Chen, S.T., et al. (2021). Tissue-resident macrophages provide a pro-tumorigenic niche to early NSCLC cells. Nature *595*, 578–584. https://doi.org/10.1038/s41586-021-03651-8.
16. Templeton, A.J., McNamara, M.G., Šeruga, B., Vera-Badillo, F.E., Aneja, P., Ocaña, A., Leibowitz-Amit, R., Sonpavde, G., Knox, J.J., Tran, B., et al. (2014). Prognostic Role of Neutrophil-to-Lymphocyte Ratio in Solid Tumors: A Systematic Review and Meta-Analysis. JNCI: J. Natl. Cancer Inst. *106*, dju124. https://doi.org/10.1093/jnci/dju124.
17. Barry, S.T., Gabrilovich, D.I., Sansom, O.J., Campbell, A.D., and Morton, J.P. (2023). Therapeutic targeting of tumour myeloid cells. Nat. Rev. Cancer *23*, 216–237. https://doi.org/10.1038/s41568-022-00546-2.
18. LaMarche, N.M., Hegde, S., Park, M.D., Maier, B.B., Troncoso, L., Le Berichel, J., Hamon, P., Belabed, M., Mattiuz, R., Hennequin, C., et al. (2024). An IL-4 signalling axis in bone marrow drives pro-tumorigenic myelopoiesis. Nature *625*, 166–174. https://doi.org/10.1038/s41586-023-06797-9.

19. Pallett, L.J., Swadling, L., Diniz, M., Maini, A.A., Schwabenland, M., Gasull, A.D., Davies, J., Kucykowicz, S., Skelton, J.K., Thomas, N., et al. (2023). Tissue CD14+CD8+ T cells reprogrammed by myeloid cells and modulated by LPS. Nature *614*, 334–342. https://doi.org/10.1038/s41586-022-05645-6.

20. Montfort, A., Colacios, C., Levade, T., Andrieu-Abadie, N., Meyer, N., and Ségui, B. (2019). The TNF Paradox in Cancer Progression and Immunotherapy. Front. Immunol. *10*, 1818. https://doi.org/10.3389/fimmu.2019.01818.

21. Croft, M. (2009). The role of TNF superfamily members in T-cell function and diseases. Nat. Rev. Immunol. *9*, 271–285. https://doi.org/10.1038/nri2526.

22. Bankhead, P., Loughrey, M.B., Fernández, J.A., Dombrowski, Y., McArt, D.G., Dunne, P.D., McQuaid, S., Gray, R.T., Murray, L.J., Coleman, H.G., et al. (2017). QuPath: Open source software for digital pathology image analysis. Sci Rep *7*, 16878. https://doi.org/10.1038/s41598-017-17204-5.

23. Backman, M., Strell, C., Lindberg, A., Mattsson, J.S.M., Elfving, H., Brunnström, H., O'Reilly, A., Bosic, M., Gulyas, M., Isaksson, J., et al. (2023). Spatial immunophenotyping of the tumour microenvironment in non–small cell lung cancer. Eur. J. Cancer *185*, 40–52. https://doi.org/10.1016/j.ejca.2023.02.012.

24. Cancer Genome Atlas Research Network (2014). Comprehensive molecular profiling of lung adenocarcinoma. Nature *511*, 543–550. https://doi.org/10.1038/nature13385.

25. Hammerman, P.S., Lawrence, M.S., Voet, D., Jing, R., Cibulskis, K., Sivachenko, A., Stojanov, P., McKenna, A., Lander, E.S., Gabriel, S., et al. (2012). Comprehensive genomic characterization of squamous cell lung cancers. Nature *489*, 519–525. https://doi.org/10.1038/nature11404.

26. Datar, I.J., Hauc, S.C., Desai, S., Gianino, N., Henick, B., Liu, Y., Syrigos, K., Rimm, D.L., Kavathas, P., Ferrone, S., and Schalper, K.A. (2021). Spatial Analysis and Clinical Significance of HLA Class-I and Class-II Subunit Expression in Non-Small Cell Lung Cancer. Clin. Cancer Res. *27*, 2837–2847. https://doi.org/10.1158/1078-0432.ccr-20-3655.

27. Montesion, M., Murugesan, K., Jin, D.X., Sharaf, R., Sanchez, N., Guria, A., Minker, M., Li, G., Fisher, V., Sokol, E.S., et al. (2021). Somatic HLA Class I Loss Is a Widespread Mechanism of Immune Evasion Which Refines the Use of Tumor Mutational Burden as a Biomarker of Checkpoint Inhibitor Response. Cancer Discov. *11*, 282–292. https://doi.org/10.1158/2159-8290.cd-20-0672.

28. Enfield, K.S.S., Colliver, E., Lee, C., Magness, A., Moore, D.A., Sivakumar, M., Grigoriadis, K., Pich, O., Karasaki, T., Hobson, P.S., et al. (2024). Spatial Architecture of Myeloid and T Cells Orchestrates Immune Evasion and Clinical Outcome in Lung Cancer. Cancer Discov. *14*, 1018–1047. https://doi.org/10.1158/2159-8290.cd-23-1380.

29. Quail, D.F., Amulic, B., Aziz, M., Barnes, B.J., Eruslanov, E., Fridlender, Z.G., Goodridge, H.S., Granot, Z., Hidalgo, A., Huttenlocher, A., et al. (2022). Neutrophil phenotypes and functions in cancer: A consensus statement. J. Exp. Med. *219*, e20220011. https://doi.org/10.1084/jem.20220011.

30. Boukhaled, G.M., Harding, S., and Brooks, D.G. (2021). Opposing Roles of Type I Interferons in Cancer Immunity. Annu. Rev. Pathol. *16*, 167–198. https://doi.org/10.1146/annurev-pathol-031920-093932.

31. Holicek, P., Guilbaud, E., Klapp, V., Truxova, I., Spisek, R., Galluzzi, L., and Fucikova, J. (2024). Type I interferon and cancer. Immunol. Rev. *321*, 115–127. https://doi.org/10.1111/imr.13272.

32. Burel, J.G., Pomaznoy, M., Lindestam Arlehamn, C.S., Weiskopf, D., da Silva Antunes, R., Jung, Y., Babor, M., Schulten, V., Seumois, G., Greenbaum, J.A., et al. (2019). Circulating T cell-monocyte complexes are markers of immune perturbations. eLife *8*, e46045. https://doi.org/10.7554/elife.46045.

33. Burel, J.G., Pomaznoy, M., Arlehamn, C.S.L., Seumois, G., Vijayanand, P., Sette, A., and Peters, B. (2020). The Challenge of Distinguishing Cell–Cell Complexes from Singlet Cells in Non-Imaging Flow Cytometry and Single-Cell Sorting. Cytom. Part A *97*, 1127–1135. https://doi.org/10.1002/cyto.a.24027.

34. Simoni, Y., Becht, E., Fehlings, M., Loh, C.Y., Koo, S.-L., Teng, K.W.W., Yeong, J.P.S., Nahar, R., Zhang, T., Kared, H., et al. (2018). Bystander CD8+ T cells are abundant and phenotypically distinct in human tumour infiltrates. Nature *557*, 575–579. https://doi.org/10.1038/s41586-018-0130-2.

35. Kortekaas, K.E., Santegoets, S.J., Sturm, G., Ehsan, I., van Egmond, S.L., Finotello, F., Trajanoski, Z., Welters, M.J.P., van Poelgeest, M.I.E., and van der Burg, S.H. (2020). CD39 Identifies the CD4+ Tumor-Specific T-cell Population in Human Cancer. Cancer Immunol. Res. *8*, 1311–1321. https://doi.org/10.1158/2326-6066.cir-20-0270.

36. Hanada, K.I., Zhao, C., Gil-Hoyos, R., Gartner, J.J., Chow-Parmer, C., Lowery, F.J., Krishna, S., Prickett, T.D., Kivitz, S., Parkhurst, M.R., et al. (2022). A phenotypic signature that identifies neoantigen-reactive T cells in fresh human lung cancers. Cancer Cell *40*, 479–493.e6. https://doi.org/10.1016/j.ccell.2022.03.012.

37. Kim, J., Park, S., Kim, J., Kim, Y., Yoon, H.M., Rayhan, B.R., Jeong, J., Bothwell, A.L.M., and Shin, J.H. (2025). Trogocytosis-mediated immune evasion in the tumor microenvironment. Exp. Mol. Med. *57*, 1–12. https://doi.org/10.1038/s12276-024-01364-2.

38. Oja, A.E., Piet, B., Zwan, D. van der, Blaauwgeers, H., Mensink, M., Kivit, S. de, Borst, J., Nolte, M.A., Lier, R.A.W. van, Stark, R., et al. (2018). Functional Heterogeneity of CD4+ Tumor-Infiltrating Lymphocytes With a Resident Memory Phenotype in NSCLC. Front. Immunol. *9*, 298. https://doi.org/10.3389/fimmu.2018.02654.

39. Steinert, E.M., Schenkel, J.M., Fraser, K.A., Beura, L.K., Manlove, L.S., Igyártó, B.Z., Southern, P.J., and Masopust, D. (2015). Quantifying Memory CD8 T Cells Reveals Regionalization of Immunosurveillance. Cell *161*, 737–749. https://doi.org/10.1016/j.cell.2015.03.031.

40. Hedrick, C.C., and Malanchi, I. (2022). Neutrophils in cancer: heterogeneous and multifaceted. Nat. Rev. Immunol. *22*, 173–187. https://doi.org/10.1038/s41577-021-00571-6.

41. Wculek, S.K., and Malanchi, I. (2015). Neutrophils support lung colonization of metastasis-initiating breast cancer cells. Nature *528*, 413–417. https://doi.org/10.1038/nature16140.

42. Saini, M., Szczerba, B.M., and Aceto, N. (2019). Circulating Tumor Cell-Neutrophil Tango along the Metastatic Process. Cancer Res. *79*, 6067–6073. https://doi.org/10.1158/0008-5472.can-19-1972.

43. Szczerba, B.M., Castro-Giner, F., Vetter, M., Krol, I., Gkountela, S., Landin, J., Scheidmann, M.C., Donato, C., Scherrer, R., Singer, J., et al. (2019). Neutrophils escort circulating tumour cells to enable cell cycle progression. Nature *566*, 553–557. https://doi.org/10.1038/s41586-019-0915-y.

44. Dickson, R.P., Erb-Downward, J.R., Martinez, F.J., and Huffnagle, G.B. (2016). The Microbiome and the Respiratory Tract. Annu. Rev. Physiol. *78*, 481–504. https://doi.org/10.1146/annurev-physiol-021115-105238.

45. Hsu-Kim, C., Hoag, J.B., Cheng, G.-S., and Lund, M.E. (2013). The Microbiology of Postobstructive Pneumonia in Lung Cancer Patients. J. Bronchology Interv. Pulmonol. *20*, 266–270. https://doi.org/10.1097/lbr.0b013e31829ddf01.

46. Littman, A.J., Jackson, L.A., and Vaughan, T.L. (2005). Chlamydia pneumoniae and Lung Cancer: Epidemiologic Evidence. Cancer Epidemiol. Biomarkers Prev. *14*, 773–778. https://doi.org/10.1158/1055-9965.epi-04-0599.

47. Jin, C., Lagoudas, G.K., Zhao, C., Bullman, S., Bhutkar, A., Hu, B., Ameh, S., Sandel, D., Liang, X.S., Mazzilli, S., et al. (2019). Commensal Microbiota Promote Lung Cancer Development via γδ T Cells. Cell *176*, 998–1013.e16. https://doi.org/10.1016/j.cell.2018.12.040.

48. El Tekle, G., and Garrett, W.S. (2023). Bacteria in cancer initiation, promotion and progression. Nat. Rev. Cancer *23*, 600–618. https://doi.org/10.1038/s41568-023-00594-2.

49. Haastert, B., Mellanby, R.J., Anderton, S.M., and O'Connor, R.A. (2013). T Cells at the Site of Autoimmune Inflammation Show Increased Potential for Trogocytosis. PLoS One *8*, e81404. https://doi.org/10.1371/journal.pone.0081404.

50. Ochs, J., Nissimov, N., Torke, S., Freier, M., Grondey, K., Koch, J., Klein, M., Feldmann, L., Gudd, C., Bopp, T., et al. (2022). Proinflammatory CD20+ T cells contribute to CNS-directed autoimmunity. Sci. Transl. Med. *14*, eabi4632. https://doi.org/10.1126/scitranslmed.abi4632.

51. Perez-Ruiz, E., Minute, L., Otano, I., Alvarez, M., Ochoa, M.C., Belsue, V., de Andrea, C., Rodriguez-Ruiz, M.E., Perez-Gracia, J.L., Marquez-Rodas, I., et al. (2019). Prophylactic TNF blockade uncouples efficacy and toxicity in dual CTLA-4 and PD-1 immunotherapy. Nature *569*, 428–432. https://doi.org/10.1038/s41586-019-1162-y.

52. Vasanthakumar, A., Liao, Y., Teh, P., Pascutti, M.F., Oja, A.E., Garnham, A.L., Gloury, R., Tempany, J.C., Sidwell, T., Cuadrado, E., et al. (2017). The TNF Receptor Superfamily-NF-κB Axis Is Critical to Maintain Effector Regulatory T Cells in Lymphoid and Non-lymphoid Tissues. Cell Rep. *20*, 2906–2920. https://doi.org/10.1016/j.celrep.2017.08.068.

53. Hwang, I., Huang, J.-F., Kishimoto, H., Brunmark, A., Peterson, P.A., Jackson, M.R., Surh, C.D., Cai, Z., and Sprent, J. (2000). T Cells Can Use Either T Cell Receptor or Cd28 Receptors to Absorb and Internalize Cell Surface Molecules Derived from Antigen-Presenting Cells. J. Exp. Med. *191*, 1137–1148. https://doi.org/10.1084/jem.191.7.1137.

54. Wetzel, S.A., McKeithan, T.W., and Parker, D.C. (2005). Peptide-Specific Intercellular Transfer of MHC Class II to CD4+ T Cells Directly from the Immunological Synapse upon Cellular Dissociation. J. Immunol. *174*, 80–89. https://doi.org/10.4049/jimmunol.174.1.80.

55. Sharma, V.J., Starkey, G., D'Costa, R., James, F., Mouhtouris, E., Davis, L., Wang, B.Z., Vago, A., Raman, J., Mackay, L.K., et al. (2023). Australian Donation and Transplantation Biobank: A Research Biobank Integrated Within a Deceased Organ and Tissue Donation Program. Transplant. Direct *9*, e1422. https://doi.org/10.1097/txd.0000000000001422.

56. Daubeuf, S., Puaux, A.-L., Joly, E., and Hudrisier, D. (2006). A simple trogocytosis-based method to detect, quantify, characterize and purify antigen-specific live lymphocytes by flow cytometry, via their capture of membrane fragments from antigen-presenting cells. Nat. Protoc. *1*, 2536–2542. https://doi.org/10.1038/nprot.2006.400.

57. Sanchez-Cespedes, M., Parrella, P., Esteller, M., Nomoto, S., Trink, B., Engles, J.M., Westra, W.H., Herman, J.G., and Sidransky, D. (2002). Inactivation of LKB1/STK11 is a common event in adenocarcinomas of the lung. Cancer Res. *62*, 3659–3662.

58. Preibisch, S., Saalfeld, S., and Tomancak, P. (2009). Globally optimal stitching of tiled 3D microscopic image acquisitions. Bioinformatics *25*, 1463–1465. https://doi.org/10.1093/bioinformatics/btp184.

59. Greenwald, N.F., Miller, G., Moen, E., Kong, A., Kagel, A., Dougherty, T., Fullaway, C.C., McIntosh, B.J., Leow, K.X., Schwartz, M.S., et al. (2022). Whole-cell segmentation of tissue images with human-level performance using large-scale data annotation and deep learning. Nat Biotech *40*, 555–565. https://doi.org/10.1038/s41587-021-01094-0.

60. Van Valen, D.A., Kudo, T., Lane, K.M., Macklin, D.N., Quach, N.T., DeFelice, M.M., Maayan, I., Tanouchi, Y., Ashley, E.A., and Covert, M.W. (2016). Deep Learning Automates the Quantitative Analysis of Individual Cells in Live-Cell Imaging Experiments. PLoS Comput. Biol. *12*, e1005177. https://doi.org/10.1371/journal.pcbi.1005177.

61. Windhager, J., Zanotelli, V.R.T., Schulz, D., Meyer, L., Daniel, M., Bodenmiller, B., and Eling, N. (2023). An end-to-end workflow for multiplexed image processing and analysis. Nat. Protoc. *18*, 3565–3613. https://doi.org/10.1038/s41596-023-00881-0.

62. Pau, G., Fuchs, F., Sklyar, O., Boutros, M., and Huber, W. (2010). EBImage—an R package for image processing with applications to cellular phenotypes. Bioinformatics *26*, 979–981. https://doi.org/10.1093/bioinformatics/btq046.

63. McLachlan (2005). Discriminant Analysis and Statistical Pattern Recognition (John Wiley & Sons).

64. Liu, N., Bhuva, D.D., Mohamed, A., Bokelund, M., Kulasinghe, A., Tan, C.W., and Davis, M.J. (2024). standR: spatial transcriptomic analysis for GeoMx DSP data. Nucleic Acids Res. *52*, e2. https://doi.org/10.1093/nar/gkad1026.

65. Robinson, M.D., and Oshlack, A. (2010). A scaling normalization method for differential expression analysis of RNA-seq data. Genome Biol. *11*, R25. https://doi.org/10.1186/gb-2010-11-3-r25.

66. Law, C.W., Chen, Y., Shi, W., and Smyth, G.K. (2014). voom: Precision weights unlock linear model analysis tools for RNA-seq read counts. Genome Biol. *15*, R29. https://doi.org/10.1186/gb-2014-15-2-r29.

67. Robinson, M.D., McCarthy, D.J., and Smyth, G.K. (2010). edgeR: a Bioconductor package for differential expression analysis of digital gene expression data. Bioinformatics *26*, 139–140. https://doi.org/10.1093/bioinformatics/btp616.

68. Smyth, G.K. (2004). Linear Models and Empirical Bayes Methods for Assessing Differential Expression in Microarray Experiments. Stat. Appl. Genet. Mol. Biol. *3*, 3–25. https://doi.org/10.2202/1544-6115.1027.

69. Phipson, B., Lee, S., Majewski, I.J., Alexander, W.S., and Smyth, G.K. (2016). Robust hyperparameter estimation protects against hypervariable genes and improves power to detect differential expression. Ann. Appl. Stat. *10*, 946–963. https://doi.org/10.1214/16-aoas920.

70. Y, B.Y.H. (1995). Controlling The False Discovery Rate - APractical. statistical *57*, 289–300. https://doi.org/10.2307/2346101.

71. McCarthy, D.J., and Smyth, G.K. (2009). Testing significance relative to a fold-change threshold is a TREAT. Bioinformatics *25*, 765–771. https://doi.org/10.1093/bioinformatics/btp053.

72. Liberzon, A., Birger, C., Thorvaldsdóttir, H., Ghandi, M., Mesirov, J.P., and Tamayo, P. (2015). The Molecular Signatures Database Hallmark Gene Set Collection. Cell Syst. *1*, 417–425. https://doi.org/10.1016/j.cels.2015.12.004.

73. Wu, D., and Smyth, G.K. (2012). Camera: a competitive gene set test accounting for inter-gene correlation. Nucleic Acids Res. *40*, e133. https://doi.org/10.1093/nar/gks461.

74. Ritchie, M.E., Phipson, B., Wu, D., Hu, Y., Law, C.W., Shi, W., and Smyth, G.K. (2015). limma powers differential expression analyses for RNA-sequencing and microarray studies. Nucleic Acids Res. *43*, e47. https://doi.org/10.1093/nar/gkv007.

75. Phipson, B., Sim, C.B., Porrello, E.R., Hewitt, A.W., Powell, J., and Oshlack, A. (2022). propeller: testing for differences in cell type proportions in single cell data. Bioinformatics *38*, 4720–4726. https://doi.org/10.1093/bioinformatics/btac582.

STAR★METHODS

KEY RESOURCES TABLE

REAGENT or RESOURCE	SOURCE	IDENTIFIER
Antibodies		
Mouse monoclonal anti-Beta-Tubulin (clone D3U1W)	Cell Signaling Technology	Cat#86298BF; RRID: AB_2715541
Rabbit monoclonal anti-CD103 (clone EPR4166[2])	Abcam	Cat#ab271889; RRID: AB_3697252
Mouse monoclonal anti-CD103 (clone BERact8)	BioLegend	Cat#350224; RRID: AB_2716189
Rabbit monoclonal anti-CD11c (clone EP1347Y)	Abcam	Cat#ab216655; RRID: AB_2864379
Rabbit monoclonal anti-CD14 (clone D7A2T)	Cell Signaling Technology	Cat##56082; RRID: AB_2799504
Mouse monoclonal anti-CD14 (clone M5E2)	BD	Cat#746304; RRID: AB_2743629
Mouse monoclonal anti-CD14 (clone M5E2)	BioLegend	Cat#301806; RRID:AB_314188
Rabbit monoclonal anti-CD16 (clone SP175)	Abcam	Cat#ab243925; RRID: AB_3697253
Mouse monoclonal anti-CD16 (clone 3G8)	BD	Cat#563784; RRID: AB_2744293
Mouse monoclonal anti-CD19 (clone SJ25C1)	BioLegend	Cat#363018; RRID:AB_2564227
Mouse monoclonal anti-CD20 (clone L26)	Cell Marque	Cat#CM120M84; RRID: AB_1158145
Mouse monoclonal anti-CD20 (clone 2H7)	BD	Cat#749954; RRID: AB_2874186
Mouse monoclonal anti-CD20 (clone 2H7)	BioLegend	Cat#302330; RRID:AB_10965543
Rat monoclonal anti-CD3 (clone CD3-12)	Abcam	Cat#ab255972; RRID: AB_3697254
Mouse monoclonal anti-CD3 (clone UCHT1)	BioLegend	Cat#300436; RRID:AB_2562124
Mouse monoclonal anti-CD3 (clone UCHT1)	BD	Cat#563725; RRID:AB_2744392
Rabbit monoclonal anti-CD39 (clone EPR20627)	Abcam	Cat#ab236038; RRID: AB_2943150
Mouse monoclonal anti-CD39 (clone TU66)	BD	Cat#742522; RRID: AB_2740840
Rabbit monoclonal anti-CD4 (clone EPR6855)	Abcam	Cat#ab181724; RRID: AB_2864377
Mouse monoclonal anti-CD4 (clone OKT4)	BioLegend	Cat#317414; RRID:AB_571959
Mouse monoclonal anti-CD4 (clone OKT4)	BioLegend	Cat#317428; RRID: AB_1186122
Mouse monoclonal anti-CD45 (clone 2B11+PD7/26)	LSBio	Cat#LS-C389721; RRID: AB_3697258
Mouse monoclonal anti-CD45 (clone 2B11+PD7/26)	LSBio	Cat#LS-C389721; RRID: AB_3697258
Mouse anti-CD45 (clone HI30)	BD	Cat#563204; RRID:AB_2738067
Mouse anti-CD45 (clone HI30)	BioLegend	Cat#304028; RRID:AB_893338
Mouse anti-CD45RA (clone PTPRC/1148)	Abcam	Cat#ab212774; RRID: AB_3697255;
Mouse anti-CD45RA (clone HI100)	BioLegend	Cat#304135; RRID: AB_11125961
Mouse anti-CD45RO (clone DCHL1)	WEHI facility	N/A
Mouse anti-CD45RO (clone UCHL1)	BD	Cat#748369; RRID:AB_2872788
Mouse anti-CD49a (clone CL7207)	Abcam	Cat#ab243032; RRID: AB_3697257
Mouse anti-CD49a (clone TS2/7)	eBiosciences	Cat#46-9490-42; RRID: AB_2573891; Clone:TS2/7
Rabbit anti-CD56 (clone MRQ-42)	Ionpath	Cat#715101-100; RRID: AB_3094828
Mouse anti-CD56 (clone HCD56)	BioLegend	Cat#318325; RRID: AB_10612566
Mouse anti-CD66b (clone G10F5)	BioLegend	Cat#305102; RRID: AB_314494
Rabbit anti-CD68 (clone D4B9C)	Cell Signaling Technology	Cat#76437BF; RRID: AB_2799882
Rabbit anti-CD69 (clone EPR21814)	Abcam	Cat#ab234512; RRID: AB_2891140

(*Continued on next page*)

Continued

REAGENT or RESOURCE	SOURCE	IDENTIFIER
Mouse anti-CD69 (clone FN 50)	BD	Cat#612818; RRID: AB_2870142
Mouse anti-CD8a (clone C8/144B)	Cell Signaling Technology	Cat#70306BF; RRID: AB_2799781
Mouse anti-CD8a (clone SK1)	eBiosciences	Cat#47-0087-42; RRID: AB_2016684
Mouse anti-CTLA4 (clone F-8)	Santa Cruz	Cat#sc-376016L; RRID: AB_10988256
Mouse anti-CTLA4 (clone 14D3)	eBiosciences	Cat#25-1529-42; RRID: AB_2573406
Mouse anti-Epcam (clone VU-1D9)	STEMCELL Technologies	Cat#60136F1
Mouse anti-Foxp3 (clone 236A/E7)	Jomar	Cat#14-4777-82; RRID: AB_467556
Mouse anti-Foxp3 (clone 206D)	BioLegend	Cat#320124; RRID: AB_2565972
Rabbit anti-GrzB (clone D6E9W)	Cell Signaling Technology	Cat#46890BF; RRID: AB_2799313
Mouse anti-GrzB (clone GB11)	BD	Cat#563388; RRID: AB_273817
Mouse anti-HLA DR (clone L243)	BioLegend	Cat#307604; RRID:AB_314682
Rabbit anti-ICOS (clone D1K2T)	Cell Signaling Technology	Cat##89601BF; RRID: AB_2800142
Hamster anti-ICOS (clone C398.4A)	BD	Cat#565881; RRID: AB_3683731
Mouse anti-IFNg (clone IFGN/466)	Abcam	Cat#ab218890; RRID: AB_2847937
Mouse anti-IFNg (clone 4S.B3)	BioLegend	Cat#502519; RRID: AB_528920
Rabbit anti-Ki67 (clone SP6)	Abcam	Cat#ab197547; RRID: AB_2924695
Mouse anti-Ki67 (clone B56)	BD	Cat#563756; RRID: AB_2732007
Mouse anti-LAG3 (clone 17B4)	ionpath	Cat#714701-100; Clone:17B4
Mouse anti-LAG3 (clone 7H2C65)	BioLegend	Cat#369203; RRID: AB_2566477
Mouse anti-MHC I (HLA ABC) (clone EMR8-5)	BD	Cat#565292; RRID: AB_2739161
Mouse anti-MHC I (clone G46–2.6)	BD	Cat#742025; RRID: AB_2871321
Rabbit anti-MHC II (HLA DR) (clone EPR3692)	ionpath	Cat#717201-100
Mouse anti-MHC II (clone G46-6[L243])	BD	Cat#612981; RRID: AB_2916889
Mouse anti-OX40 (clone ACT35)	Cell Signaling Technology	Cat#98785BF; RRID: AB_2800308
Mouse anti-OX40 (clone BER-ACT35)	BioLegend	Cat#350029; RRID: AB_2632863
Rabbit anti-PD1 (clone D4W2J)	Cell Signaling Technology	Cat#86163BF; RRID: AB_2728833
Mouse anti-PD1 (clone EH12.2H7)	BioLegend	Cat#329906; RRID: AB_940483
Rabbit anti-PDL1 (clone E1L3N)	Cell Signaling Technology	Cat#13684BF; RRID: AB_2687655
Mouse anti-PDL1 APC (clone 29E.2A3)	BioLegend	Cat#329707; RRID: AB_940358
Mouse anti-PanCK (clone AE1/AE3)	Abcam	Cat#ab80826; RRID: AB_1640401
Mouse anti-TCR a/b BV605 (clone IP26)	BioLegend	Cat#306732; RRID:AB_2650819
Rabbit anti-TIM3 (clone D5D5R)	Cell Signaling Technology	Cat#45208BF; RRID: AB_2716862
Mouse anti-Tim3(CD366) (clone F38-2E2)	eBiosciences	Cat#15-3109-41; RRID: AB_2802204
Rabbit anti-Tryptase (clone EPR9522)	Abcam	Cat#ab271916; RRID: AB_2910584
Rabbit anti-Vimentin (clone D21H3)	Cell Signaling Technology	Cat#5741BF; RRID: AB_10695459
Mouse anti-dTCR (clone H-41)	Santa Cruz	Cat#sc-100289L; RRID: AB_3095826
dsDNA (clone 3519DNA)	ionpath	Cat#708901-100
Biological samples		
Patient samples	Victorian Cancer Biobank	N/A
Patient samples	Australian Donation and Transplant Biobank	N/A
Patient samples	Volunteer Biospecimen Donor Registry	N/A
Chemicals, peptides, and recombinant proteins		
Hoechst 33342	Thermo Scientific	Cat#62249; RRID:AB_3675235
Live/Dead - Propidium Iodide	Sigma	Cat#P4170
Streptavidin APC	BioLegend	Cat#405207
Collagenase I	Worthington	Cat#LS004197

(*Continued on next page*)

Continued

REAGENT or RESOURCE	SOURCE	IDENTIFIER
Critical commercial assays		
Foxp3/Transcription Factor Staining Kit	eBiosciences	Cat#00-5523-00
Deposited data		
Image Mass Cytometry data from 39 LUAD and 23 LUSC samples	Enfield et al.[29]	https://doi.org/10.5281/zenodo.12587543
Image Mass Cytometry data from 416 LUAD samples	Sorin et al.[13]	https://doi.org/10.5281/zenodo.7760826
MIBI and GeoMx data generated for this paper	This paper	https://doi.org/10.5281/zenodo.17051521
TCR sequencing data	This paper	https://doi.org/10.5281/zenodo.17051521
Oligonucleotides		
Sequencing primers are presented in Table S4	This paper	N/A
Software and algorithms		
FlowJo	Tree Star	RRID:SCR_008520
QuPath	Bankhead et al.[22]	RRID:SCR_018257
GeoMx DSP Data Analysis Suite	https://nanostring.com/products/geomx-digital-spatial-profiler/geoscript-hub/	RRID:SCR_021660
XGBoost	https://xgboost.ai/	RRID:SCR_021361
Python scripts to run cell-classification pipeline that uses XGBoost	This paper	https://github.com/WEHI-SODA-Hub
R Studio	RStudio, Inc	RRID:SCR_000432
R	R Project for Statistical Computing	RRID:SCR_001905
R packages limma, edgeR, imcRtools, scater, BiocParallel, SingleCellExperiment, SpatialExperiment, standR, speckle, SummarizedExperiment	Bioconductor	RRID:SCR_001905
R packages dplyr, ggplot2, ggpubr, ggrepel, pheatmap, viridis, RColorBrewer, scales, stringr, tidyr, tidyverse, rmarkdown, survival, survminer, purrr	CRAN	RRID:SCR_003005
R scripts for figure generation	This paper	https://github.com/WEHI-labatlab/lung-mibi-cd14cd4

EXPERIMENTAL MODEL AND STUDY PARTICIPANT DETAILS

Human samples

Written informed consent was obtained from all patients by the Victorian Cancer Biobank prior to inclusion in the study, according to protocols approved by the WEHI Human Research Ethics Committee (HREC, 10/04LR). Human tonsil FFPE tissues were used for antibody validation. NSCLC specimens and associated clinical data were obtained from the Victorian Cancer Biobank from treatment-naïve, surgically resected early-stage lung cancer patients (Stage I to IIIa). Patients, both male and female, were classified as ever-smokers (current and ex-smokers who had quit smoking at least 1 year prior to sample collection) or never-smokers (lifetime smoking of less than 100 cigarettes). Only patients with an overall survival (OS) of less than 3 years post-surgery and with OS of more than 6 years post-surgery were included in the study. Human tissues from non-cancer patients were obtained from male and female deceased organ donors, at the time of organ acquisition for transplantation through the Australian Donation and Transplant Biobank[55] (HREC/4814/Austin-2019). All donors were free of cancer, hepatitis B, and hepatitis C, and were HIV negative. PBMC used for the trogocytosis experiments were collected from male and female healthy donors through the Victorian Blood Donor Registry (HREC 10/04LR). Patient and organ donor details are described and summarized in Tables S1 and S2 (n = 64). Three formalin-fixed paraffin-embedded (FFPE) serial sections (4μm thickness) were cut for H&E staining, MIBI proteomic experiment on gold-coated slides (Ionpath #567001), and for GeoMX transcriptomic experiment.

Non-small cell lung cancer imaging datasets

Data from Sorin et al.[13] were available on Zenodo (https://doi.org/10.5281/zenodo.7383627). Data from Enfield et al.[28] were kindly provided by the authors under a Data Transfer Agreement (https://doi.org/10.5281/zenodo.12587543).

METHOD DETAILS

Human lung and tumor tissue dissociation

Lung and tumor samples were either processed immediately or held intact for a maximum of 16 h at 4°C in DMEM/F12 media (Gibco) supplemented with 1 mg/mL of penicillin and streptomycin (Invitrogen). Surgical samples were minced then digested for 1 h at 37°C with 2 mg/mL collagenase I (Worthington, #LS004197) and 200 U/mL deoxyribonuclease (Worthington, #LS002140) in 0.2% D-glucose (Sigma) in DPBS (Gibco), as previously described.[5] The cell suspension was filtered through 100 μm strainer (Falcon) and washed with 2% FCS-PBS, followed by red blood cell lysis and further washing with 2% FCS-PBS to obtain a single cell suspension. Single cell suspensions were either stained immediately for flow cytometry analysis or cryopreserved in 90% FCS:10% DMSO and stored in liquid nitrogen prior to staining.

Flow cytometry

Cells were stained with fixable viability dye Zombie NIR (Biolegend) for 15 min. Cells were washed with 2%FCS-PBS, then blocked with anti-CD16/32 FCRγ antibody (WEHI antibody facility) for 10 min. Cells were stained with extracellullar antibodies for 30 min at 4°C. Cells were then fixed and permeabilized with Foxp3/Transcription Factor Staining Kit (eBiosciences) and stained with intracellular antibodies for 30 min at 4°C. Samples were resuspended in FACS buffer (2% FCS in PBS) and data acquired using an Aurora spectral unmixing cytometer (CyTEK). Interrogation of singlet and doublet cells was performed by staining cells with extracellular antibodies for 30 min 4°C then incubated with Hoechst 33342 (5μg/ml) for 30min at °C. Samples were acquired using a BD Symphony flow cytometer. Data were analyzed using FlowJo (Tree Star).

Image cytometry

Real time images were captured using BD FACSDiscover S8 Cell Sorter running BD FACSChorus acquisition software (BD Biosciences, San Jose). The instrument contains 5 lasers with 6 spatially separated laser intercepts (the blue laser is split to support full-spectrum detection at one intercept and BD CellView imaging detection at a second intercept. Live cells were gated on CD45-PE^{+}CD3-BV570^{+}CD4-RB545^{+}. The images for each cell were captured in real-time with the following detectors and bandpass filters, light-loss, forward scatter, side scatter (488/15), Image Channel 1 (534/46, CD4), and image channel 3 (788/225, CD14). Co-localization of CD4 and CD14 were determined using the imaging data and the following image analysis, Max Intensity (CD14 BB700) vs. Correlation (CD4 RB545/CD14 BB700) plot.

Trogocytosis

The protocol was adapted from Daubeuf et al.[56] In brief, peripheral blood mononuclear cells (PBMCs) were isolated from healthy donors and stained with an antibody cocktail to sort CD3^{+}TCRαβ^{+}CD14^{-} and CD3^{-}TCRαβ^{-}CD14^{-}HLA-DR^{+} cell populations. Following cell sorting, each subset was independently labeled with 1 μg/mL of biotinylated membrane dye (EZ-Link Sulfo-NHS-LC-Biotin, Catalog #21335) in PBS for 10 min at 25°C. An equal volume of fetal calf serum (FCS) was then added, and the cells were incubated for an additional 10 min at 4°C. Subsequently, the biotin-labeled cells were co-cultured with unlabelled cells at a 1:1 ratio (total 1×10^{6} cells) at 37°C for 4 h. The cells were acquired using NovoCyte Penteon Flow cytometer and analyzed using FlowJo 10.9.0. For TNF-α treatment, 100ng/μL stock solution of recombinant human TNFα (catalog # ab9642) was prepared in dPBS. Appropriate volume of the stock solution was added to 4 h co-culture experiment described above so that the final concentration of TNFα was 10 or 80ng/mL.

TCR sequencing

CD45^{+}CD3^{+}CD4^{+} CD14^{+}or CD14^{-} T cells were sorted on the Aria Fusion (BD) and DNA extracted using DNeasy Blood & Tissue kit (Qiagen). DNA Integrity was measured on the Tapestation 4200 (Agilent). Samples with a DNA Integrity Number >8.5 were sent for TCRβ sequencing by ImmunoSeq (Adaptive Biotechnologies, Seattle). TCR reads and sequences were analyzed on the Immunoseq data analysis platform (Adaptive Biotechnologies).

Oncogenic driver mutation sequencing

EGFR, KRAS and *STK11* mutation analyses were performed on fresh frozen tumor samples. Genomic DNA was prepared using the Qiagen DNeasy Blood and Tissue kit (Qiagen #69504) according to manufacturer's instructions. Sequencing was performed using a 2-step PCR approach for targeted sequencing. Unique primer sequences for *EGFR, KRAS* and *STK11* that contain a common overhang sequence at the 5′ end were used to amplify *EGFR, KRAS* and *STK11* exonic regions of interest. Cycling conditions were initial denaturation at 96°C for 5min, 18 cycles of denaturation at 96°C for 30s, annealing at 57°C for 30s, and elongation at 72°C for 30s, followed by a final elongation step at 72°C for 5min. PCR amplicons were purified using 1.0x Ampure Beads (Beckman Coulter) prior to the second PCR to introduce adaptor sequences and 8 bp dual-index barcodes for multiplexing. Cycling conditions were initial denaturation at 95°C for 3min, 24 cycles of denaturation at 95°C for 15s, annealing at 60°C for 30s, and elongation at 72°C for 30s, followed by a final elongation step at 72°C for 7min. The barcoded PCR product size was assessed by agarose gel electrophoresis, purified using 0.8x Ampure Beads and quantified by Qubit fluorometry (ThermoFisher Scientific). PCR products from up to 96 samples were pooled equimolar and sequenced on a MiSeq (Illumina). Read pairs were demultiplexed according to the index

sequences using bcl2fastq, and subsequently processed by Trim_galore (https://www.bioinformatics.babraham.ac.uk/projects/trim_galore/) to remove adaptors and low-quality reads. The clean reads were aligned using the https://sarah-d.shinyapps.io/crispr-indel/, to WT sequence from NCBI RefSeq Genome database GRCh38. Primer sequences are detailed in Key Resource Table (Uppercase: overhang sequences for multiplexing). For *STK11,* we screened mutations in *STK11* exon 1 and 2, as these are associated with worse survival in NSCLC patients.[57] We investigated the presence of previously described alterations in exon 1 *Q37Ter* and *K44Ter* and screened for mutations in all of exon 2. For *EGFR* we evaluated *ex19-del*, *L858R*, and *T790M* mutations. For *KRAS*, we assessed mutations in G12 and G13 codons.

GeoMx data collection

FFPE sections from 64 NSCLC samples were sent to the NanoString Center of Excellence in Spatial Biology (Griffith University) for sample processing and data collection on the GeoMx platform (Nanostring). Slides were baked at 60°C for 90 min and deparaffinised at 72°C for 30min, Heat-induced epitope retrieval for 20 min and Proteinase K treatment (1μg/mL) for 15 min using the automated LEICA BOND Rx system. Immunofluorescent staining was performed using the morphology antibodies from Nanostring Solid Tumor Morphology kit: SYTO13 (nucleus, 1:10 dilution), PanCK-AF532 (tumor cells, 1:40 dilution) and CD45-AF594 (immune cells, 1:40 dilution). For *in situ* hybridization for next generation sequencing, tissue sections were then hybridized with Whole Transcriptome Atlas (WTA; Lot# HWTA21003) probes for 16 h at 37°C in a humidity-controlled chamber. Two segments were collected: PanCK positive cells and CD45 positive cells, with a minimum of 200 cells collected for each individual area of illumination (AOI). A total of 345 AOIs were collected.

Validation of 38-plex antibody panel for MIBI

Rare earth polymer conjugated antibodies were purchased from Ionpath or conjugated to metal polymers according to manufacturer protocol (Ionpath). Briefly, 100μg of carrier-free antibody was reduced with 4mM TCEP. Partially reduced antibody was then incubated at 37°C for 1h with the metal-loaded polymer. The antibody concentration was quantified by measuring the IgG absorbance at 280nm on the NanoDrop. The conjugated antibody was eluted to obtain a final concentration of 0.5mg/ml. All antibodies were first validated by immunohistochemistry on NSCLC tissue sections. Panels of conjugated antibodies were then evaluated on human tonsils to ensure specificity and the absence of isobaric and isotopic overlap. Antibodies were then titrated on lung cancer tissues before being pooled in a 38-plex panel for staining of the complete cohort (Figure S1A).

Slide staining and scanning on MIBI

Slides were processed as per manufacturer protocol and stained with our bespoke 38-plex antibody panel. Antigen retrieval was performed with Tris EDTA pH9 (Agilent, #S236784-2) using the PT Link Module (Thermo Scientific), sections blocked with 10% donkey serum and stained overnight with 36 conjugated antibodies (all except Tryptase and CD20 antibodies). Slides were then washed in TBS-0.1% Tween and stained for 30 min with Tryptase and CD20 antibodies before being dehydrated and post-fixed with 2% glutaraldehyde. Slides were stored in a vacuum chamber before scanning. Fields of view of 400 × 400μm (1024x1024 pixels) were acquired at a dwell time of 1ms. The mass-spec pixel data generated is automatically converted into TIFF images. MIBI images were pre-processed for isobaric correction using MIBI/O (Ionapth) and visualized on QuPath.[22] Adjacent FOVs were stitched together using a groovy script plugin in QuPath.[58]

QUANTIFICATION AND STATISTICAL ANALYSIS

Single-cell segmentation and classification on MIBI data

Cell segmentation was performed using a QuPath extension applying Deep Cell model Mesmer.[59,60] The dsDNA channel was used as the nuclei feature. The matrix addition of the median normalized Major histocompatibility Complex Class I (MHC-I) and pan-cytokeratin (panCK) channels were used as the membrane features. Segmented cells with a nuclei area of <50 pixels and cells touching the border of images were removed.

Cell classification was performed using the supervised method XGBoost. We manually annotated 52,719 cells on 116 FOVs using in-house developed tools on QuPath. Cells were annotated as epithelial cells, stromal cells, B cells, $CD4^+$ T cells, $CD8^+$ T cells, Treg cells, NK cells, $\gamma\delta$T cells, macrophages, dendritic cells, neutrophils, mast cells, or others. Annotations were assigned to cells based on the shape and intensity of the markers within the cell boundaries visible on the images. All markers were used to train the model. Each marker was measured in four compartments: nucleus, cytoplasm, membrane, and the entire cell. In each cell compartment, the measurements calculated were mean, standard deviation, and the 0.7, 0.8, 0.9, 0.95, 0.96, 0.97, 0.98, 0.99, 0.995, 0.999 quantiles. A polynomial feature generation of degree two was used between markers expected to be co-expressed. The combinations were generated from pools of markers expected to be co-expressed. These features were generated on cell mean measurements of the markers. In total 1713 features were used to train the model. To compensate for the imbalanced data, we used the synthetic minority oversampling technique (SMOTE). To select the hyper-parameters, we used the Bayesian search cross validation (https://scikit-optimize.github.io/stable/modules/generated/skopt.BayesSearchCV.html). In assessing the results of the training confusion matrices, scores such as f1, balanced accuracy, ROC AUC score, were used. A second independent model was developed for

determining positive or negative expression of individual functional markers for each cell type. A suite of Nextflow pipelines has been implemented to automatically train and tune the Machine Learning classification model (XGBoost) used after manual annotations.

Tissue classifier and immune subgroup classification

Twelve different pixel classifiers were trained in QuPath and applied to our cohort of 64 patients to delimit the tumor and stroma area. For spatial analysis, three compartments were created: tumor core, border and stroma where the border was defined as 40μm inside and outside the tumor area. Patients were grouped into myeloid-, lymphoid-myeloid- or lymphoid-enriched (M-, LM-, L-enriched) after an unsupervised k mean (k = 3) clustering of the proportions of lymphoid and myeloid cells in each sample.

Cell neighborhood clustering of immune cells

Cell neighborhood (CN) clusters of immune cells were defined by first determining the 10 closest neighbors (excluding itself) of every cell. The cell type frequencies were determined and converted into proportions. These proportions were used in a K-means clustering with k = 7. Cell type proportions have been *Z* score normalized within each cluster.

Sorin et al. and Enfield et al. analysis

The same k-means clustering (k = 3) used in our cohort was applied to both datasets using their cell classification grouping of myeloid and lymphoid cells in each patient. To delimitate the 'in' and 'out' tumor area in Sorin et al., a cell neighborhood analysis was performed using **imcRtools** package (version 1.14).[61] Interaction graphs based on the cell's locations were constructed using distance-based expansion with radius 30, and then neighbors were aggregated by cell type (top hierarchical level: Cancer, Endothelial cells, Immune cells and Others) and k-means clustering was performed with k = 4. All the cells within two clusters mainly composed of tumor cells were classified as inside the tumor area.

To define cells as CD14 positive we first expanded nuclear boundaries provided by Sorin et al. by 3 pixels using functionality of the **EBImage** R package[62] and re-calculated the mean intensity of CD14 for each cell. To define CD14-positive cells among non-monocytes, we employed a data-driven classification approach based on CD14 expression profiles in annotated monocyte populations. Classical monocytes ($CD14^+CD16^-$) were used as the positive reference group, and non-classical monocytes ($CD14^-CD16^+$) as the negative reference group, reflecting high and low CD14 expression levels, respectively.

For each group, we estimated the empirical density of CD14 expression using kernel density estimation (KDE) with Gaussian kernel. The log-density ratio (LDR) was then computed at each expression value for all patients together. The LDR reflects the relative likelihood that a given CD14 expression value originates from an expected CD14 positive cell (classical monocyte) rather than a non-classical monocyte, which we expect to be CD14 negative. To account for the imbalance in group sizes (with classical monocytes substantially outnumbering non-classical monocytes), we adjusted the classification threshold using the log of the observed group size ratio. This choice reflects a Bayesian decision-theoretic framework with prior probabilities proportional to group sizes and a 0–1 loss function, yielding a threshold that minimizes expected misclassification under class imbalance.[63] Cells with CD14 expression levels yielding an LDR greater than this threshold were classified as CD14 positive.

To calculate minimal distances to cells of interest ($CD14^{+/-}CD4^+$ T cells), we used the *minDistToCells* function of the **imcRtools** package (version 1.14). Based on this distance, cells that are further than 50 units away from the cells of interest were excluded from the neighborhood analysis presented in Figures 5E and 5F. Significant differences in immune cell type composition of neighborhoods between $CD14^+$ and $CD14^-$ $CD4^+$ T cell were assessed using a *propeller* test from the **speckle** Bioconductor R package (version 1.2)[64].

Cell-cell interactions were counted and tested using the *testInteractions* function of the **imcRtools** package. Interactions were counted using the "classic" method on the cell-interaction graph built based on a 30μm radius expansion. Heatmap shows the summed significance scores for each cell type pair across all 113 images. For each IMC image, cell type pairs were assigned a score based on spatial interaction: 1 for interaction (red), 0 for no interaction or avoidance (white), and −1 for avoidance (blue). These scores were then summed across all images, resulting in a range from −31 to 113.

Cell neighborhood clustering of immune cells in Sorin et al. was performed as per our cohort by using k-means clustering with k = 6.

GeoMx data analysis

NanoString GeoMx DSP data was processed with GeoMx DSP Data Analysis Suite (https://nanostring.com/products/geomx-digital-spatial-profiler/geoscript-hub/). All downstream analysis was performed in the R statistical programming language (version 4.3.2) using predominantly Bioconductor packages (version 3.18). Further quality control was performed using the **standR** Bioconductor R package version 1.6.[64] Library sizes were normalized with the TMM method,[65] as implemented in the *geomxNorm* function of the **standR** package. Count data were transformed to log2-counts per million, voom precision weights were estimated and linear models for differential expression analysis were fitted using **edgeR**'s *voomLmFit* function with additional cyclicloess normalization (**edgeR** version 4.0).[66,67] For the comparison of LUAD and LUSC cancer types, age and gender were included as covariates in the linear model. Differential expression was assessed using moderated t-statistics[68] with robust empirical Bayes variance estimation.[69] Genes with a false discovery rate <0.05 and log-fold-change threshold >1.1 were defined as significantly differentially expressed using TREAT.[70,71] For LUAD M vs. LLM comparison, the cancer sub-types, age and smoking status were included in the linear model. Genes were ranked using *p*-values obtained from moderated t-statistics. The top ranked genes with a log-fold change < −0.5 and

>0.5 are highlighted in the mean-difference plot. For the comparison of $CD14^+$-high vs. $CD14^+$-low tumors, CD14 status was included in the linear model together with smoking status. CD14 status was determined as high/low using the MIBI data and defined as areas of illumination (AOI) with greater/smaller percentage of CD14 positive cells than the median value across all AOI. Gene set testing to test for enrichment of REACTOME gene sets, Gene Ontology terms, KEGG pathways and Hallmark gene sets from the Molecular Signatures Database (MSigDB)[72] was performed using the *camera* function in **limma** Bioconductor R package (version 3.58).[73,74] For Figures 6E and S4B, genes from selected pathways were highlighted using barcode plots, where the x axis represents ordered moderated t-statistics from the testing procedure described above. Significant differences in proportions of cells with higher expression of functional markers between $CD14^+$ and $CD14^-$ were assessed using a *propeller* test from the **speckle** Bioconductor R package (version 1.2).[75]

Statistical analysis

Statistical analyses were performed using R (2023.06.1 + 524). Boxplots present median ± standard deviation. Non-normal data were compared between two groups using Wilcoxon rank-sum test. Samples with less than 5 cells of the cell type of interest were excluded from the analysis. The significance between two groups in Kaplan Meier survival curves was calculated using log rank (Mantel-Cox) test. In the heatmaps, percentages are calculated for each patient and then *Z* score normalized across all patients using the scale function with default parameters in R., Statistical details including *n*, mean, dispersion measure, and statistical tests are included in the figure legend for each experiment and plot.